

Proton Conducting Sulfonated Poly(ionic liquid)

Block Copolymers

Rui Sun,¹ Mahesh Agrawal,¹ Kenneth C. Neyerlin,³ Joshua D. Snyder,² Yossef A. Elabd^{1*}

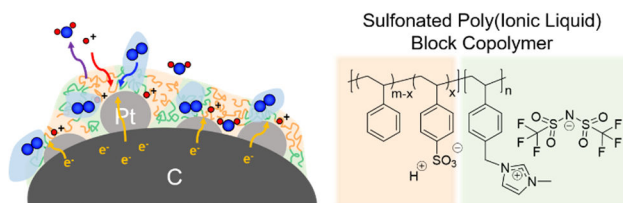
¹Department of Chemical Engineering, Texas A&M University, College Station, TX 77843

²Department of Chemical and Biological Engineering, Drexel University, Philadelphia, PA 19104

³Chemistry and Nanoscience Center, National Renewable Energy Laboratory, Golden, CO 80401, USA

*Corresponding author to be addressed; email: elabd@tamu.edu.

For Table of Content Use Only



ABSTRACT: Herein, we report the synthesis of proton-conducting sulfonated poly(ionic liquid) block copolymers (S-PILBCPs) containing one block with sulfonic acid (sulfonated styrene: SS) and the other with an IL moiety (vinylbenzylmethylimidazolium bis(trifluoromethylsulfonyl)imide: VBMIm-TFSI) using reversible addition-fragmentation chain-transfer (RAFT) polymerization and post-polymerization modifications (*i.e.*, functionalization, anion exchange reactions, and sulfonation). The S-PILBCPs uniquely conjoin the SS block with mobile protons (H^+) and the PIL block with mobile anions (TFSI $^-$), where multiple highly desired properties, including high proton conductivity (from the SS block), and high IL-philicity and oxygen solubility (from the PIL block) can exist compartmentally within a microphase separated morphology (evidenced by differential scanning calorimetry (DSC) and small-angle X-ray scattering (SAXS)). High ion conductivity of 79.7 mS/cm at a PIL block composition of 21.6 mol% was observed at 80 °C and 90% relative humidity (RH) (comparable to the benchmark Nafion ionomer). This work successfully demonstrates the design of S-PILBCPs as a new material platform and showcases its promise as an ionomer for proton exchange membrane fuel cells (PEMFCs) as they simultaneously and compartmentally combine proton conductivity and oxygen solubility. These benefits have recently been leveraged to achieve substantial improvement in oxygen reduction reaction (ORR) activity and subsequently fuel cell performance.

1. Introduction

Proton exchange membrane fuel cells (PEMFCs) are promising alternative energy solutions that have received significant attention for their potential to achieve high power densities and high energy densities at low operating temperature with zero local greenhouse gas emission, specifically in automotive applications.¹ However, the expensive cell components, primarily the required high content of noble metal in the electrocatalysts (primarily platinum (Pt) and platinum-group-metals (PGM)), remains a major obstacle to achieve cost-effective PEMFCs for light duty vehicles.² Currently, the benchmark cathode PGM loading for a commercial PEMFC vehicle is *ca.* 0.4 mg_{Pt} cm⁻² (*e.g.*, 0.365 mg_{Pt} cm⁻² for Toyota Mirai).^{3, 4} The required high content of Pt catalyst is primarily the result of sluggish oxygen reduction reaction (ORR) in the acidic environment at the cathode. With the recent development of advanced alloy electrocatalysts⁵⁻⁷ and an improved understanding in integration,⁸ substantial progress has been achieved in minimizing the cathode Pt loading.⁹ However, significant loss in fuel cell performance has been observed at reduced cathode Pt loadings (<0.1 mg_{PGM} cm⁻²), attributed to increased charge and mass transport resistances.¹⁰

Figure 1a shows a schematic of the structure of porous catalyst layer at the-cathode wherein the electrochemical reactions occur. As illustrated in the schematic, ORR only occurs at triple phase boundaries between the ionomer (proton transport pathways), the carbon-supported catalyst particles (electron conduction), and the porous network (O₂ transport pathways).¹¹ With decreasing Pt loading and available Pt area, increased proton and O₂ fluxes are transported to limited catalyst sites, resulting in local transport resistances with impeded O₂ transport and reduced ORR activities.^{2, 12} Local transport resistances are related to the ionomer film surrounding the catalyst sites (illustrated by the spring-like structure in Figure 1b and Figure 1c), which is assumed to be a

sum of the two interfacial resistances between the gas/ionomer and ionomer/Pt site, and the bulk resistance of the confined ionomer thin film.¹²

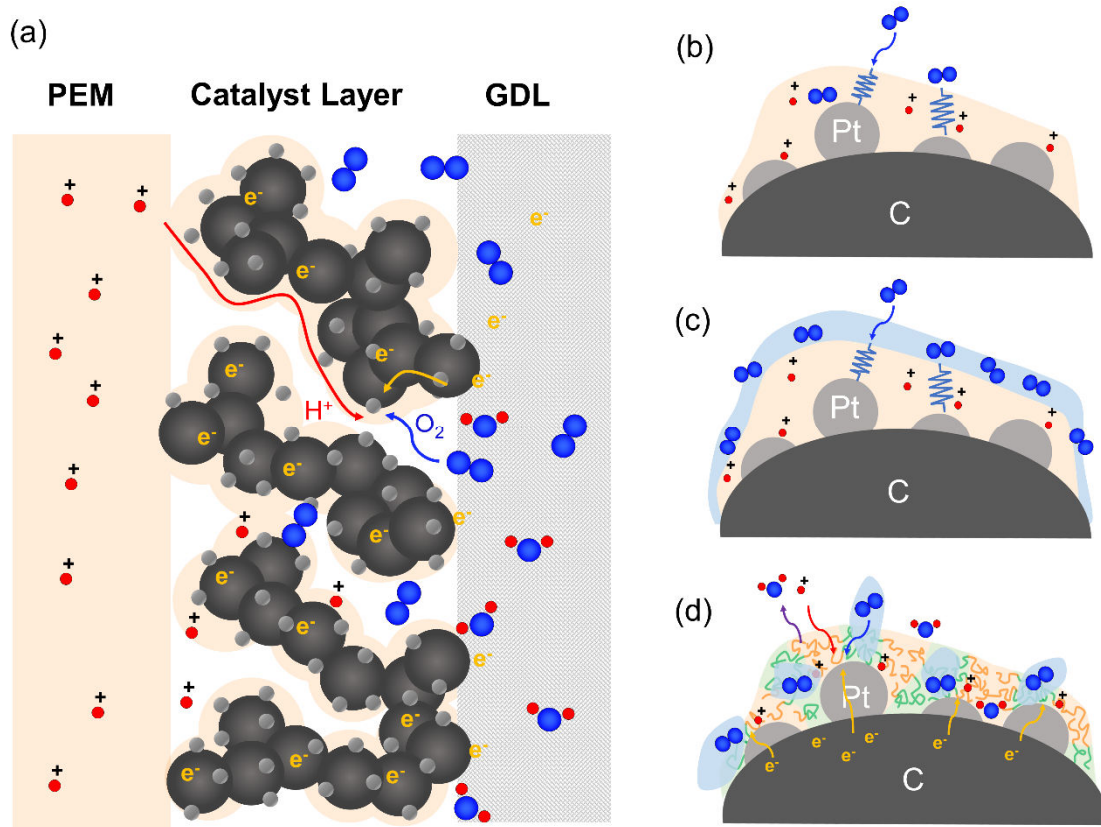


Figure 1. (a) Schematic of the porous cathode catalyst layer structure between the PEM and the gas diffusion layer (GDL) wherein the electrochemical reactions occur. Local transport to a Pt site through (b) conventional ionomer (c) conventional ionomer/ionic liquid (d) S-PILBCP ionomer/ionic liquid, where the transported species are represented as proton (\bullet^+), water ($\bullet\bullet$), oxygen ($\bullet\bullet$).

Recently, ionic liquids (ILs) have exhibited potential as effective electrocatalyst additives for improving the ORR activity in half-cell electrochemical measurements.¹³⁻²⁴ A study by Snyder *et*

*al.*¹⁴ first reported that ORR activity was enhanced by 2 to 3 times *via* the incorporation of hydrophobic IL with high O₂ solubility into nanoporous PtNi electrocatalysts. Zhang *et al.*^{15, 16} also demonstrated that the ORR performance and stability can be efficiently boosted by IL modification and the catalytic activity is strongly correlated with the degree of IL filling, as well as the alkyl chain length of the cations (*i.e.*, imidazolium). Hypothesized mechanisms for the increased ORR activity and stability include: (1) the high O₂ solubility in IL results in higher effective O₂ concentration at the catalytic surface and further improves Pt utilization,^{19, 20} (2) the hydrophobic ILs facilitate the expulsion of excess water to achieve more free active catalyst sites,²¹ and (3) ILs serve as a reaction medium to prevent local ORR byproduct build-up and protect active sites from being poisoned.^{22, 23} However, to date, the full kinetic advantage of the IL has yet to be fully realized in full PEMFC tests in a membrane electrode assembly (MEA) due to the difficulty in the conformal deposition of IL throughout the catalyst layer. Specifically, the benchmark ionomer for PEMFCs, *i.e.*, Nafion, has a relatively low O₂ solubility and low IL-philicity (*i.e.*, low affinity with free IL). Local transport resistances might be increased due to the possible interfacial resistance between the IL thin layer and Nafion (illustrated in Figure 1c), leading to significant mass transport losses.¹⁸ In addition, Nafion sulfonate adsorption on the surface of Pt catalyst has been widely reported in literature.^{2, 24-27} The sulfonate adsorption could potentially poison the Pt surface, resulting in ionomer adsorption and confinement on Pt surface (physical barriers to oxygen transport). Recently, IL interlayers demonstrate the ability to mitigate the sulfonate adsorption of Nafion on Pt by physical exclusion of the sulfonate from the catalyst surface or electrostatic screening of the electrode surface or of the sulfonate groups by IL ions.²⁴ Hence, it will be of great interest to design novel ionomers with higher IL-philicity as an alternative of Nafion to facilitate the incorporation of free IL in the catalyst layer. Desired ionomers are expected

to: (1) achieve ion transport properties on par with the benchmark Nafion ionomer for proton conduction, (2) improve free IL retention and minimize any detrimental losses at the interface between a free IL and ionomer, (3) minimize the interfacial O₂ transport resistance with improved catalyst/ionomer interface, and (4) mitigate the sulfonate adsorption on Pt surface.

Specifically, two categories of ionomers that have attracted particular attention in electrochemical energy applications are sulfonated block copolymers and poly(ionic liquid) block copolymers (PILBCPs). Sulfonated block copolymers (containing sulfonic acid in one block) have been intensively explored as proton conducting membranes and ionomers for PEMFCs.²⁸⁻³⁴ More recently, PILBCPs (containing IL chemistry in one block) have been designed and applied as solid polymer electrolytes for batteries and hydroxide conducting membranes and ionomers for alkaline fuel cells.³⁵⁻⁴⁵ Conjoining these two materials into one, *i.e.*, sulfonated PIL block copolymers (S-PILBCPs), where one block consists of IL chemistry and the other contains sulfonic acid, is of significant interest to provide a new material platform with desired properties such as high proton conductivity (from the sulfonated block) and IL-philicity (from the PIL). Proton could be transported through the hydrophilic sulfonated domain and O₂ could diffuse through the hydrophobic PIL/IL domain to react with the electrons at the triple phase boundary, resulting in enhanced Pt utilization. Advantages such as high electrochemical stability, more favorable O₂ diffusivity and solubility, moderate water uptake and water transport properties, enhanced humidity tolerance, optimal interface with ILs, and a broad library of chemistries for the IL block may also be achieved. To date, the synthesis of S-PILBCPs still remains an unexplored area of research, where the only S-PILBCP was reported by Meek and Elabd,⁴⁶ consisting of a styrene-based sulfonic acid block with mobile lithium (Li⁺) cations and an acrylate-based PIL block with mobile bis(trifluoromethylsulfonyl)imide (TFSI⁻) anions (both are hydrophobic domains). This

study is the first report on the synthesis of a proton conducting (H^+) S-PILBCP with mobile protons (hydrophilic domain) and TFSI⁻ anions (hydrophobic domains), where recently this S-PILBCP has demonstrated successful improved ORR and fuel cell performance.^{47, 48}

Herein, we report the synthesis of a proton-conducting S-PILBCP containing a styrene-based sulfonic acid block with mobile protons (H^+) and a styrene-based PIL block with mobile TFSI⁻ anions *via* reversible addition-fragmentation chain transfer (RAFT) polymerization and post-polymerization modifications. The thermal properties, morphology, ion conductivity, and water transport of the S-PILBCPs were investigated at three different PIL compositions. Note that, the morphology, ion conductivity, and water transport were studied with bulk films. Despite it is not a very close mimic of ionomer binder layer in terms of thickness, this study investigated the synthesis and transport properties of the S-PILBCPs, elucidating their potential as novel ionomers for PEMFCs with enhanced ORR activity and fuel cell performance.

2. Experimental

2.1. Materials

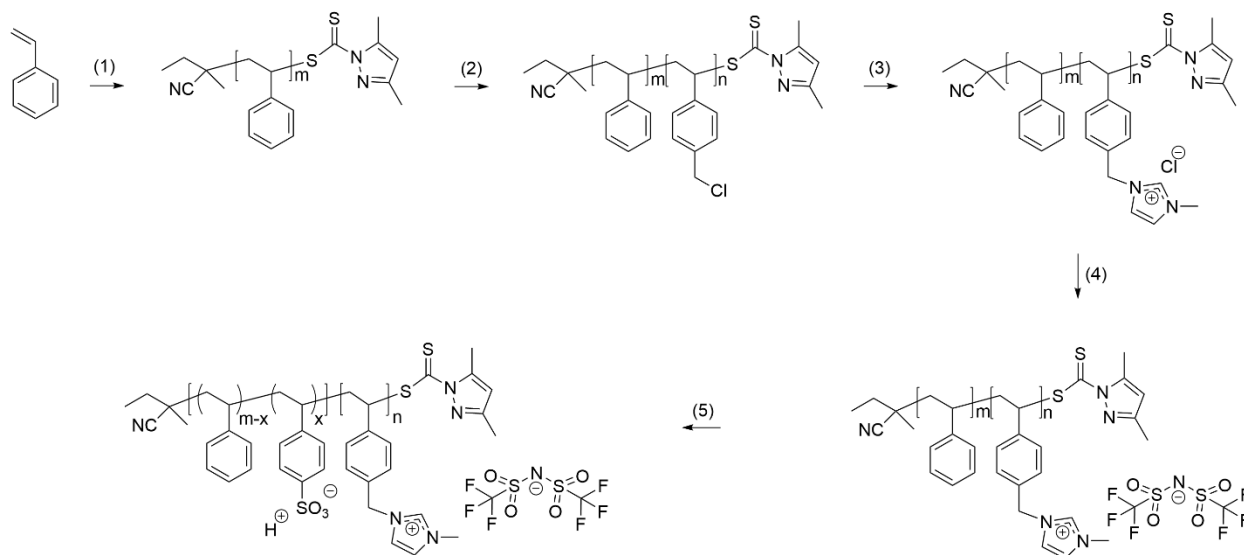
2-cyanobutanyl-2-yl 3,5-dimethyl-1*H*-pyrazole-1-carbodithioate (chain transfer agent (CTA), $\geq 95\%$) was used as received from Boron Molecular. 4-cyano-4-(phenylcarbonothioylthio)pentanoic acid (CTA, $\geq 95\%$), toluene (anhydrous, 99.8%), tetrahydrofuran (THF, anhydrous, $\geq 99.9\%$), methanol (ACS reagent, $\geq 99.8\%$), 4-vinylbenzyl chloride (VBC, 90%), *N,N*-dimethylformamide (DMF, ACS reagent, $\geq 99.8\%$), *N*-methylimidazole (MIm, ReagentPlus®, 99%), acetone (ACS reagent, $\geq 99.5\%$), hexane (anhydrous, 95%), bis(trifluoromethane) sulfonimide lithium salt (LiTFSI, 99.95% trace metals basis), acetic anhydride (ReagentPlus®, $\geq 99\%$), sulfuric acid (ACS reagent, 95.0–98.0%), dichloromethane (DCM, ACS reagent, $\geq 99.5\%$), chloroform-*d*

(CDCl₃, 99.96 atom % D, contains 0.03 % (v/v) TMS), acetonitrile-*d*₃ (ACN-*d*₃, ≥ 99.8 atom% D), and dimethyl sulfoxide-*d*₆ (DMSO-*d*₆, 99.9 atom % D, contains 0.03% v/v TMS) were used as received from Sigma-Aldrich. Bis(trifluoromethanesulfonyl)imide (HTFSI, > 99.0%) was used as received from TCI chemicals. Styrene (ReagentPlus®, contains 4-tert-butylcatechol as stabilizer, ≥ 99%, Sigma-Aldrich) was purified by passing through inhibitor remover (for removing tert-butylcatechol, Sigma-Aldrich) prior to polymerization. 2,2'-azobis(2-methylpropionitrile) (AIBN, 98%) and 1,1'-azobis(cyclohexanecarbonitrile) (VAZO-88, 98%, Sigma-Aldrich) were recrystallized twice in methanol. Deionized (DI) water with resistivity *ca.* 16MΩ cm was used as appropriate. Acetyl sulfate was synthesized in accordance with literature procedures.⁴⁹

2.2. Synthesis of polystyrene (PS) macro-chain transfer agent (macro-CTA)

RAFT polymerization was utilized to synthesize PS macro-CTA (Scheme 1(1)). Reaction procedure for synthesizing PS macro-CTA for poly(SS-H-*b*-VBMIm-TFSI-35.5) is given as follows: 250.63 g of styrene (2.41 mol) and 6.0855 g of CTA (0.0240 mol) were added into 250.06 g toluene in a 1 L three-neck round bottom flask equipped with a condenser. At room temperature, the solution was purged with nitrogen for 1 h. The mixture was then heated to reach reflux and reacted for 22 h under continuous nitrogen purge. The product was twice precipitated in methanol, filtered, and then dried under vacuum at room temperature for 24 h. Yield: 120.48 g of solid particles. ¹H NMR (500 MHz, CDCl₃, 23 °C) δ (ppm): 7.25–6.27 (m, C₆H₅), 2.15–1.70 (m, CH₂–CH), 1.70–1.15 (m, CH₂–CH) (NMR, Figure 2(I)); SEC (THF, 40 °C): M_n = 5.36 kg mol⁻¹, *D* = M_w/M_n = 1.17 (against PS standards) (SEC, Figure S1, Supporting Information). Poly(SS-H-*b*-VBMIm-TFSI-21.6) was synthesized using 4-cyano-4-(phenylcarbonothioylthio)pentanoic acid as CTA. Poly(SS-H-*b*-VBMIm-TFSI-48.8) was synthesized using 2-cyanobutanyl-2-yl 3,5-

dimethyl-1H-pyrazole-1-carbodithioate as CTA. Detailed synthesis procedure of PS macro-CTAs for poly(SS-H-*b*-VBMIm-TFSI-21.6) and poly(SS-H-*b*-VBMIm-TFSI-48.8) can be found in Supporting Information.



Scheme 1. Synthesis of proton-conducting S-PILBCPs. (1) styrene, CTA (2-cyanobutanyl-2-yl 3,5-dimethyl-1*H*-pyrazole-1-carbodithioate), toluene or THF, reflux, 22 h; (2) PS macro-CTA, VBC, AIBN, THF, reflux, 5 h; (3) *N*-methylimidazole, DMF, 80 °C, 48 h; (4) LiTFSI, DMF, 50 °C, 48 h; (5) DCM, acetyl sulfate, reflux, 5 h. Poly(SS-H-*b*-VBMIm-TFSI-21.6) was synthesized using 4-cyano-4-(phenylcarbonothioylthio)pentanoic acid as CTA.

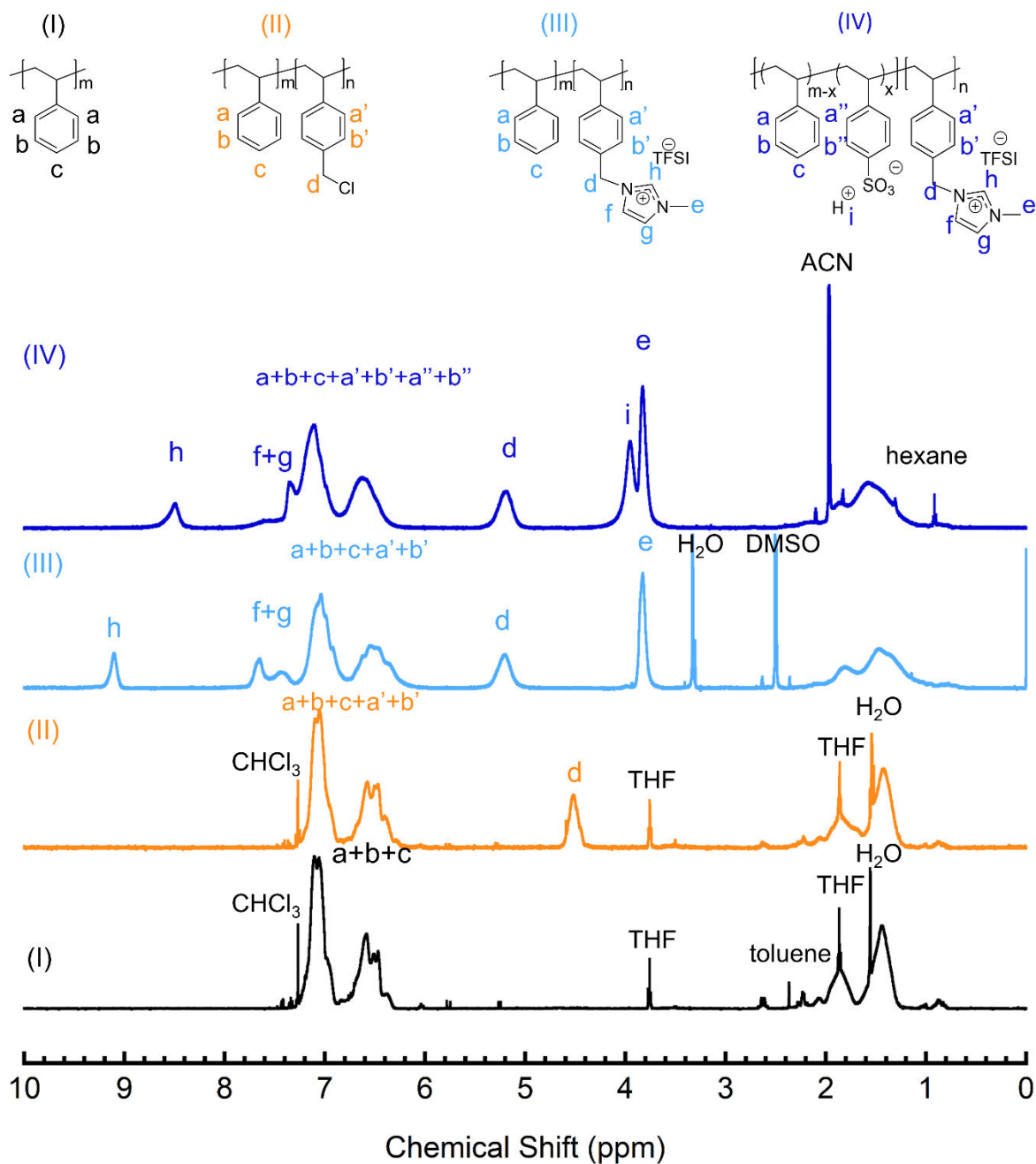


Figure 2. ^1H NMR spectra of poly(SS-H-*b*-VBIm-TFSI-35.5) and related precursors: (I) polystyrene (black) (II) poly(S-*b*-VBC) (orange) (III) poly(S-*b*-VBIm-TFSI) (light blue) (IV) poly(SS-H-*b*-VBIm-TFSI) (dark blue).

2.3. Synthesis of poly(*S-b-VBC*) diblock copolymer

The non-ionic diblock copolymer, poly(*S-b-VBC*), was prepared by RAFT polymerization (Scheme 1(2)). An example of the reaction procedures is shown as follows: 50.05 g of PS macro-CTA (9.3 mmol) and 142.73 g of VBC (0.94 mol) were added into 133.70 g THF in a 500 mL three-neck round bottom flask equipped with a condenser. The mixture was stirred under continuous nitrogen purge at room temperature for 1 h and then heated to reach reflux. Subsequently, 0.1539 g of AIBN (0.94 mmol) was dissolved in 9.00 g of THF and purged for 5 min under nitrogen before injecting in the reactant mixture. After reacting for 5 h under reflux and static nitrogen purge, the product was twice precipitated and extensively washed in methanol, filtered, and then dried under vacuum at room temperature for 24 h. Yield: 79.0217 g of solid particles. ^1H NMR (500 MHz, CDCl_3 , 23 °C) δ (ppm): 7.25–6.15 (m, C_6H_5 and C_6H_4), 4.67–4.30 (m, $\text{C}_6\text{H}_4\text{-CH}_2\text{-Cl}$), 2.15–1.15 (m, $\text{CH}_2\text{-CH}$, $\text{CH}_2\text{-CH}$) (NMR, Figure 2(II)); $M_n = 9.48 \text{ kg mol}^{-1}$ (from ^1H NMR analysis).

2.4. Synthesis of poly(*S-b-VBIm-TFSI*) diblock copolymer

The ionic diblock copolymer, poly(*S-b-VBIm-TFSI*) [VBIm-TFSI = vinylbenzylmethyylimidazolium bis(trifluoromethanesulfonyl)imide], was synthesized by the quaternization of non-ionic polymer precursor poly(*S-b-VBC*), followed by anion exchange with LiTFSI (shown in Scheme 1(3) and 1(4)). An example of the reaction procedures is shown as follows: 20.0050 g of poly(*S-b-VBC*) (0.057 mol of VBC) was dissolved in 70 mL DMF in a 125 mL flask. 17.45 g (0.213 mol) of 1-methylimidazole (VBC/1-methylimidazole, 1/3.7 mol/mol) was added dropwise to the mixture. The reaction was carried out at 80 °C for 48 h and terminated by precipitation in hexane. Subsequently, the polymer was extensively washed in hexane and

acetone and dried under vacuum at room temperature for at least 24 h. Yield: 26.2975 g solid particles (105 %; yield in excess of 100% due to residual acetone). Poly(S-*b*-VBMIm-Cl) was then ion exchanged to TFSI⁻ form (Scheme 1(4)) by first dissolving 10.0052 g of poly(S-*b*-VBMIm-Cl) (0.024 mol of Cl⁻) in 20 mL of DMF. Solution of 10.78 g (0.038 mol) of LiTFSI in 10 mL of DMF were added dropwise into the polymer solution (Cl⁻/TFSI⁻ = 1/1.6 mol/mol). The reaction was carried out at 50 °C for 48 h and terminated by precipitating the reaction mixture in 440 mL of water/methanol (1/1 v/v). The anion exchanged polymer, poly(S-*b*-VBMIm-TFSI), was washed multiple times with DI water for 72 h, filtered, and dried under vacuum at room temperature for 24 h. Yield: 14.2754 g of solid polymer (90.4 %). ¹H NMR (500 MHz, DMSO-*d*₆, 23 °C) δ (ppm): 9.27–8.93 (s, N-CH=N), 7.81–7.29 (s, N-CH=CH-N), 7.29–6.02 (m, C₆H₄ and C₆H₅), 5.43–4.87 (m, C₆H₄-CH₂-N), 3.92–3.60 (s, N-CH₃), 2.30–0.60 (m, CH₂-CH, CH₂-CH) (NMR, Figure 2(III)). Elemental analysis (EA) calculated: C, 53.04; H, 4.45; N, 6.29; Cl, 0.00; S, 9.59; F, 17.05. Found: C, 51.80; H, 4.43; N, 6.65; Cl, 0.00; S, 10.08; F, 16.17.

2.5. Synthesis of poly(SS-H-*b*-VBMIm-TFSI) diblock copolymer

Poly(SS-H-*b*-VBMIm-TFSI) (H refers to proton or acid form of sulfonated styrene) was synthesized by the sulfonation of poly(S-*b*-VBMIm-TFSI) in accordance with a literature procedure⁴⁹ (Scheme 1(5)). Poly(S-*b*-VBMIm-TFSI) (2.0013 g) was dissolved in dry dichloromethane (40 mL) to achieve a 5% (w/v) solution. The sulfonation reaction was started by adding acetyl sulfate solution (1/1 mol acid/mol S; 0.9006 g acetic anhydride, 0.5376 g H₂SO₄ in 10 mL of dry dichloromethane) dropwise into the solution under reflux. The solution appeared dark brown after reacting for 5 h. 5 mL of methanol was slowly added into the reaction mixture to stop the reaction. The sulfonated polymer was then precipitated and washed with hexane, followed

by drying under vacuum at room temperature for 24 h. 0.9952 g of the precipitate was then purified by washing with 20 mL HTFSI aqueous solution for 24 h twice (2/1 mol HTFSI/mol SS; 1.27 g HTFSI) followed by drying in a vacuum oven at room temperature for 12 h. Yield: 0.862 g of solid particles. ^1H NMR (500 MHz, $\text{ACN-}d_3$, 23 °C) δ (ppm): 8.82–8.21 (s, N–CH=N), 7.87–7.26 (s, N–CH=CH–N), 7.26–6.09 (m, C_6H_4 , C_6H_5), 5.45–4.79 (m, $\text{C}_6\text{H}_4\text{-CH}_2\text{-N}$), 4.32–3.86 (s, H^+) 3.86–3.55 (s, N–CH₃), 2.50–0.70 (m, CH₂–CH, CH₂–CH) (NMR, Figure 2(IV)). EA calculated (based on 40% sulfonation): C, 48.80; H, 4.09; N, 5.78; S, 12.03; F, 15.69. EA Found: C, 47.76; H, 4.25; N, 5.98; S, 11.17; F, 16.27.

2.6. Characterization

The molecular weight and molecular weight distribution of PS macro-CTA was determined by size exclusion chromatography (SEC) with a Waters SEC system equipped with a THF Styragel column (Styragel@HR 5E, effective separation of molecular weight range: 2 to 4000 kg mol⁻¹) and a 2414 refractive index (RI) detector. SEC was calibrated using PS standards (M_w : 2.97 to 983 kg mol⁻¹) and the experiments were conducted using THF as mobile phase (flow rate: 1.0 mL/min) at 40 °C. Proton nuclear magnetic resonance spectroscopy (^1H NMR; Varian 500 MHz spectrometer, 23 °C) was conducted for chemical analysis with various deuterium solvents. ^1H NMR spectra of PS macro-CTA and poly(S-*b*-VBC) were performed referencing to CDCl_3 at 7.27 ppm. ^1H NMR spectra of poly(S-*b*-VBMIm-Cl) and poly(S-*b*-VBMIm-TFSI) were performed referencing to $\text{DMSO-}d_6$ at 2.50 ppm. ^1H NMR spectra of the poly(SS-H-*b*-VBMIm-TFSI) were performed referencing to $\text{ACN-}d_3$ at 1.94 ppm. EA was conducted by Atlantic Microlab, Inc., Norcross, GA.

A Fourier transform infrared (FTIR) spectrometer (Nicolet 6700 Series; Thermo Electron Corporation) equipped with a single reflection diamond attenuated total reflection (ATR) accessory (Specac; Quest) was used to perform infrared spectroscopy. All infrared spectra were collected using a liquid nitrogen-cooled mercury-cadmium-telluride (MCT) detector at 32 scans per spectrum, a resolution of 4, and data spacing of 1.928 cm^{-1} . The collected spectra were corrected with a background subtraction of the spectrum of the bare ATR crystal.

Glass transition temperatures (T_g s) were measured by differential scanning calorimetry (DSC; TA Instruments, Q200) under a N_2 environment (50 mL/min) over a temperature range of $-140\text{ }^\circ\text{C}$ to $200\text{ }^\circ\text{C}$ (heating/cooling rate: $10\text{ }^\circ\text{C}/\text{min}$). T_g was determined on the second heating cycle thermogram using the mid-point method. Thermal degradation temperatures (T_{ds}) were measured by thermal gravimetric analysis (TGA; TA Instruments, Q50) under nitrogen environment (60 mL/min) from 20 to $900\text{ }^\circ\text{C}$ (heating rate: $10\text{ }^\circ\text{C}/\text{min}$). T_d was determined at 5 % weight loss of the polymers after the initial loss of atmospheric moisture.

Small-angle X-ray scattering (SAXS) profiles were collected with a Rigaku SMAX-3000 instrument. Characteristic Cu X-rays with a wavelength (λ) of 1.542 \AA was generated at 40 kV and 30 mA by a rotating copper anode (MicroMax-007HFM, Rigaku). The X-rays were focused, monochromated, and collimated using a Confocal Max-Flux double-focusing optic and subsequent pinhole collimation. The SAXS data were collected by a Gabriel-type 2D multi-wire detector at a sample-to-detector distance of 1.5 m and calibrated with silver behenate. SAXS experiments were performed with exposure times ranging from 900 to 3600s under vacuum at room temperature. The raw data were corrected for transmission and background noise, then averaged azimuthally to give intensity as a function of momentum transfer magnitude, $I(q)$, where $q = 4\pi (\sin \theta)/\lambda$ and 2θ is the scattering angle (q range: 0.07 nm^{-1} - 3 nm^{-1}). The intensities were reported in arbitrary units

(a.u.). Data was analyzed by Igor Pro v8.04 (WaveMetrics, Inc) with procedures from Argonne National Laboratory.^{50, 51} The films for SAXS experiments were prepared by first dissolving PILBCPs in solvents (acetone for poly(S-*b*-VBMIm-TFSI) and ACN for poly(SS-H-*b*-VBMIm-TFSI), respectively) to produce a 20% w/w polymer solution. The solutions were subsequently cast on Mylar substrates and kept in an enclosed environment at room temperature for 48 h with three open 10 mL beakers of solvents, *i.e.*, solvent-evaporation. Subsequently, the films were dried under vacuum at room temperature for 24 h and annealed at 100 °C for 48 h. The Mylar substrates were removed prior to SAXS measurements.

2.8. Ion Conductivity

The ionic conductivities of poly(SS-H-*b*-VBMIm-TFSI) were measured using electrochemical impedance spectroscopy (EIS; Solartron, 1260 impedance analyzer, 1287 electrochemical interface, Zplot software) with an AC amplitude of 10 mV over a frequency range of 0.1 – 10⁶ Hz. In-plane conductivity were measured by a four-electrode configuration (BekkTech LLC, BT-112). Temperature- and humidity-dependent conductivities were measured under controlled temperature and humidity in an environmental chamber (Espec, BTL-433 model). Samples were exposed to the corresponding temperature and humidity for at least 2 h to achieve equilibrium conditions. Conductivity was determined by the following equation:

$$\sigma = L_{electrodes}/AR \quad (1)$$

where $L_{electrodes}$ is the distance between two inner electrodes, and A is the cross-sectional area of the polymer film ($A = Wl$; W is the film width and l is the film thickness), and R is the real impedance obtained from the Nyquist plot (x-intercept of the semicircle regression over a high

frequency range). Six conductivity measurements were performed at each equilibrium conditions and an average value of these steady-state measurements is reported.

The films for conductivity experiments were prepared by first dissolving poly(SS-H-*b*-VBMIm-TFSI) in ACN to make a 5% w/w polymer solution and cast onto glass substrates (*ca.* 30 mm (length) \times 7 mm (width) \times 1 mm (thickness)). The films were cast in an enclosed ambient environment for 24 h and then dried in vacuum oven at room temperature for 12 h prior to conductivity measurements. The film thicknesses were averages of six repeated measurements by a Mitutoyo digital micrometer (\pm 1 μ m accuracy). The thickness of the films for conductivity measurements are *ca.* 30 - 50 μ m.

2.9. Water Vapor Sorption

Water vapor sorption (*S*) was investigated with dynamic vapor sorption (DVS; TA Instruments, Q5000) at controlled temperatures and humidity. To remove any residual water in the sample, powder samples were preconditioned at 60 °C and 0% RH in the DVS until equilibrium was established (*i.e.*, $<$ 0.05 wt% change for at least 30 min) for all conditions. Subsequently, the relative humidity was systematically adjusted to 30%, 45%, 60%, 75%, and 90% RH at 60 °C, and then maintained at 90% RH, while temperature was systematically changed to 50 °C, 40 °C, and 30 °C, equilibrating at each condition. The polymer water vapor equilibrium sorption (*S*) [wt%, g H₂O/g dry polymer] was determined by the following equation:

$$S = \frac{W - W_0}{W_0} \times 100 \quad (2)$$

where W_0 and W are dry and wet polymer weights measured before and after the DVS experiment, respectively.

Water vapor sorption kinetics was investigated with DVS at controlled water activities. Free-standing films were first preconditioned at 0% RH and the corresponding temperature until equilibrium was reached (*i.e.*, < 0.05 wt% change for at least 30 min) at all temperatures. Activity was then changed from 0.1 to 0.9 by systematically applying step changes of 0.1 and maintained at the condition until sorption equilibrium was established. After reaching equilibrium, the activity was increased by 0.1 almost instantaneously (reference and sample humidity reached the new activity within 1 min). Measurements were performed for each sample at 30, 40, 50 and 60 °C, respectively, and repeated for each sample at each temperature three times.

The water vapor solubility [$\text{g}_{\text{water}} / \text{g}_{\text{polymer}}$] was calculated by $(W-W_0)/W_0$, where W_0 is dry polymer weight measured when equilibrium was reached after preconditioned at 0% RH and W is wet polymer weight measured when sorption equilibrium was established after each water activity change. Sorption kinetic data were represented as the normalized mass intake $M(t)/M_{\text{eq}}$, which is the ratio between the mass sorption at time t and at equilibrium (eq), and were regressed to the analytical solution of the one-dimensional mass continuity equation for planar coordinates with constant mass boundary conditions following the method reported in literature^{52, 53}:

$$\frac{M(t)}{M_{\text{eq}}} = \frac{m(t)-m_0}{m_{\text{eq}}-m_0} = 1 - \frac{8}{\pi^2} \sum_{n=0}^{\infty} \frac{1}{(2n+1)^2} \exp[-Df^2 t] \quad (3)$$

$$f = \frac{(2n+1)\pi}{2l}, n=0, 1, 2, \dots \infty \quad (4)$$

where m_0 and l are the initial polymer weight at $t = 0$ and the polymer film thickness, respectively. D is the diffusion coefficient of water vapor in the polymer, which is the only adjustable parameter in the regression.

The films for water vapor sorption kinetic experiments were prepared by first dissolving poly(SS-H-*b*-VBMIm-TFSI) in ACN to produce a 10% w/w polymer solution. Polymer solutions were cast onto Mylar substrates in an enclosed environment at room temperature for 48 h with

three open 10 mL beakers of solvents. The films were then dried in a vacuum oven at room temperature for 12 h. The Mylar substrates were removed prior to water sorption measurements. The film thicknesses reported were averages of three repeated measurements by a Mitutoyo digital micrometer with $\pm 1 \mu\text{m}$ accuracy. The thickness of the films for water vapor sorption kinetic experiments were *ca.* 100 - 400 μm .

3. Results and Discussion

A series of sulfonated styrene-based PIL block copolymers (S-PILBCPs) were synthesized at various compositions with two sequential ionic blocks, where one block consists of a partially sulfonated polystyrene with tethered sulfonate anion (SO_3^-) and mobile proton (H^+), and another block consists of a styrene-based PIL with tethered *N*-heterocyclic imidazolium cation (MIm^+) and mobile hydrophobic anion (TFSI^-) (Table 1). This series of S-PILBCPs were synthesized *via* a five-step synthetic pathway: (1,2) sequential RAFT polymerization, (3) post-functionalization reaction, (4) anion exchange reaction, and (5) sulfonation reaction (Scheme 1). The chemistry of the S-PILBCPs and precursors was characterized using ^1H NMR spectroscopy and the NMR spectra for the non-sulfonated and sulfonated PILBCP at a specific composition are shown in Figure 2. Different from our previous work⁴⁶ (a sulfonated acrylated-based PIL block copolymer with Li^+ counter cations instead of H^+ counter cations), sequential RAFT polymerization was performed under reflux in this study to synthesize the non-ionic styrene-based diblock copolymer (*i.e.*, poly(S-*b*-VBC)) at a larger scale (*ca.* 80 g). PS was first synthesized as macro-CTAs with molecular weights of 6.32 kg mol^{-1} , 5.36 kg mol^{-1} , and 4.63 kg mol^{-1} , respectively (Figure S1, Supporting Information). Poly(S-*b*-VBC) was then synthesized targeting approximately 80 repeat units in total with different PIL block volume fractions. The VBC block molar composition in

poly(S-*b*-VBC) (Table 1) was determined from the relative integration ratio of proton resonances of the methylene group in VBC at 4.30–4.67 ppm (CH_2-Cl , labeled (d)) to the sum of all aromatic proton resonances at ortho (a and a'), meta (b and b'), and para positions (c) (*i.e.*, $\frac{5d}{d+2(a+b+c+a'+b')}$) (Figure 2(II)). After the functionalization, the presence of the protons and methyl group of the imidazolium rings was observed in NMR spectra of all PILBCPs, indicating the functionalization reactions were successfully performed. The integration ratio of the imidazolium ring protons at C(4,5) (f, g) positions (7.29–7.81 ppm) to the aromatic protons (6.02–7.29 ppm) (*i.e.*, $\frac{5(f+g)}{(f+g)+2(a+b+c+a'+b')}$) (Figure 2(III)) matched with the composition of VBC block in the neutral polymers, indicating all PILBCPs were fully functionalized. Additionally, elemental analysis (EA) was conducted to confirm the efficacy of the anion exchange reactions. A close match of the experimental and theoretical compositions of the anion exchanged PILBCPs was observed with negligibly small chloride content, indicating the polymers were successfully exchanged to TFSI form. The molecular weights of the TFSI-conducting PILBCPs, poly(S-*b*-VBMIm-TFSI), can be calculated from the molecular weight of PS, PIL block molar composition, and the chemical structure of poly(S-*b*-VBMIm-TFSI) (Table 1). The sulfuric acid group was then introduced onto the aromatic ring of PS block *via* sulfonation, following similar procedure in literature.⁴⁹ Note that, a color change to brown was observed after the sulfonation reaction. The presence of the protons on the imidazolium ring (Figure 2(IV)) were still observed at a similar chemical shift in S-PILBCPs compared to the spectra prior to sulfonation (Figure 2(III)), indicating the retention of PIL chemistry after sulfonation. Degree of sulfonation was estimated to be *ca.* 40 mol% by comparing the EA results before and after sulfonation. The NMR spectra of PILBCPs with PIL block molar composition of 21.6% and 48.8% are shown in Supporting Information (Figure S2 and S3, Supporting Information).

Table 1. PIL block copolymers (non-sulfonated and sulfonated) composition and thermal properties.

PILBCPs ^a	mol % ^a	vol % ^b	M _n (kg mol ⁻¹) ^c	T _d (°C) ^d	T _{g1} (°C) ^e	T _{g2} (°C) ^e
Poly(S- <i>b</i> -VBMIIm-TFSI-21.6)	21.6	48.4	13.99	337	40	98
Poly(S- <i>b</i> -VBMIIm-TFSI-35.5)	35.5	65.6	18.30	350	37	89
Poly(S- <i>b</i> -VBMIIm-TFSI-48.8)	48.8	76.8	23.80	345	37	84
Poly(SS-H- <i>b</i> -VBMIIm-TFSI-21.6)	-	-	-	240	-	113
Poly(SS-H- <i>b</i> -VBMIIm-TFSI-35.5)	-	-	-	253	36	107
Poly(SS-H- <i>b</i> -VBMIIm-TFSI-48.8)	-	-	-	283	36	94

^aNumbers correspond to PIL block mol % determined from ¹H NMR spectroscopy. ^bVolume fractions calculated from density of polystyrene (1.04 g cm⁻³) and PIL homopolymer (1.40 g cm⁻³ for poly(VBMIIm-TFSI), calculation can be found in Supporting Information). ^cDetermined from the molecular weight of PS (SEC), PIL block composition (¹H NMR), and the chemical structure of poly(S-*b*-VBMIIm-TFSI). ^dDetermined by 5% polymer weight loss after subtracting the initial loss of atmospheric moisture. ^eDetermined by DSC using mid-point method.

Infrared spectra (Figure 3a) and TGA thermograms (Figure 3b) further confirmed the chemistry of the S-PILBCPs and their precursors. The characteristic infrared bands of the TFSI anion were observed in the non-sulfonated PILBCPs after anion exchange prior to the sulfonation (*i.e.*, SO₂ asymmetric stretching: 1348 cm⁻¹, 1329 cm⁻¹, SO₂ symmetric stretching: 1133 cm⁻¹; CF₃ stretching: 1226, 1180 cm⁻¹; S-N-S stretching bands: 1053 cm⁻¹), which is closely matched with previous literature.^{54, 55} After sulfonation, the characteristic infrared bands of TFSI anion remain in the spectra and two additional peaks appeared at 1035, 1006 cm⁻¹ (indicated by the arrows in Figure 3a), representing the symmetric stretching vibrations of the sulfonate group and the in-plane

bending vibrations of the phenyl ring (in styrene) para-substituted with the sulfonate group, respectively.^{49, 56} Figure 3b shows the TGA thermograms of the S-PILBCPs and non-sulfonated PILBCPs with TFSI anion at a specific composition and Table 1 lists the thermal decomposition temperatures (T_d s) of all polymers. The non-sulfonated PILBCPs are thermally stable with an onset T_d of 337, 350, 345 °C for PIL block molar compositions of 21.6%, 35.5%, 48.8%, respectively. After sulfonation, a decrease of the onset T_d was observed in S-PILBCPs with all three compositions, further confirming the success of the sulfonation reactions. The weight loss up to 200 °C can be resulted from the release of water molecules from the S-PILBCPs due to the increased hydrophilicity after sulfonation. The extended temperature range for water release could be resulted from the strong interaction between the absorbed water molecules and the sulfonic acid groups.⁵⁷ The weight loss between 250 and 340 °C can be attributed to the cleavage of the sulfonate from the styrene rings, consistent with previous studies on sulfonated PS.⁵⁷ Infrared spectra and TGA thermograms of the S-PILBCPs and non-sulfonated PILBCPs with PIL block molar compositions of 21.6% and 48.8% are shown in Supporting Information (Figure S5 and S6, Supporting Information).

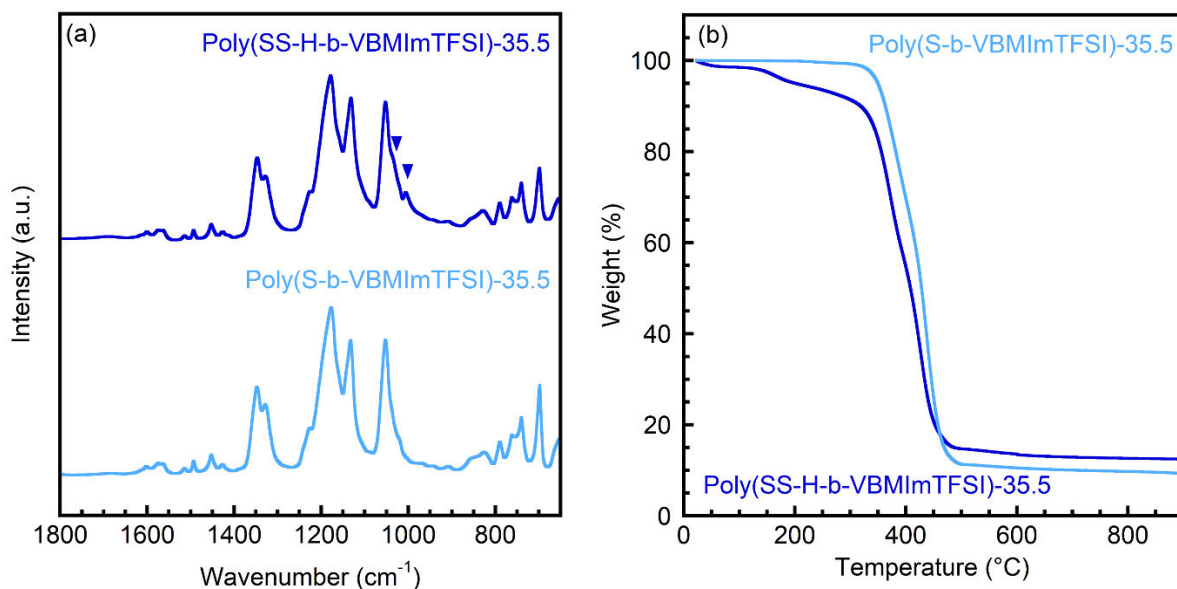


Figure 3. (a) ATR-FTIR spectra and (b) TGA thermograms of poly(SS-H-*b*-VBmIm-TFSI-35.5) and related non-sulfonated PILBCP: poly(SS-H-*b*-VBmIm-TFSI-35.5) (dark blue) and poly(S-*b*-VBmIm-TFSI-35.5) (light blue). Arrows represent the characteristic infrared bands of the sulfonate group.

Figure 4 shows the DSC thermograms of the S-PILBCPs and non-sulfonated PILBCPs at three separate compositions and Table 1 lists the glass transition temperatures (T_g s) of all polymers. The non-sulfonated PILBCPs, poly(S-*b*-VBmIm-TFSI), exhibit two distinct T_g s (Figure 4a), where the lower T_g (*ca.* 37 °C) corresponds to the PIL block (*i.e.*, poly(VBmIm-TFSI)) and the higher T_g (84 to 98 °C) corresponds to the PS block, suggesting microphase separation of the non-sulfonated poly(S-*b*-VBmIm-TFSI) diblock copolymers. The DSC thermograms for poly(SS-H-*b*-VBmIm-TFSI) are shown in Figure 4b. After sulfonation, two distinct T_g s can be found at higher PIL block composition (*i.e.*, poly(SS-H-*b*-VBmIm-TFSI-35.5) and poly(SS-H-*b*-VBmIm-TFSI-48.8)), while only one T_g is measurable for poly(SS-H-*b*-VBmIm-TFSI-21.6) with lower PIL block

composition. The T_g s of the PIL block were observed at 36 °C, consistent with the non-sulfonated PILBCPs prior to sulfonation in Figure 4a. The disappearance of the PIL block T_g in poly(SS-H-*b*-VBMIm-TFSI-21.6) might be attributed to the increasing ion interaction after sulfonation and the relatively low PIL block composition, where the glass transition of PIL block may not be detected as a distinct T_g . The T_g s of the partially sulfonated PS block were found in all three compositions (*i.e.*, 113 °C, 107 °C, 94 °C for PIL molar compositions of 21.6%, 35.5%, 48.8%, respectively) of the S-PILBCPs and increased approximately 15 °C compared to the T_g s of PS block before sulfonation, as a result of the addition of the polar sulfonate group tethered to the aromatic ring. These results suggest that microphase separation is maintained even after the sulfonation at high PIL block composition.

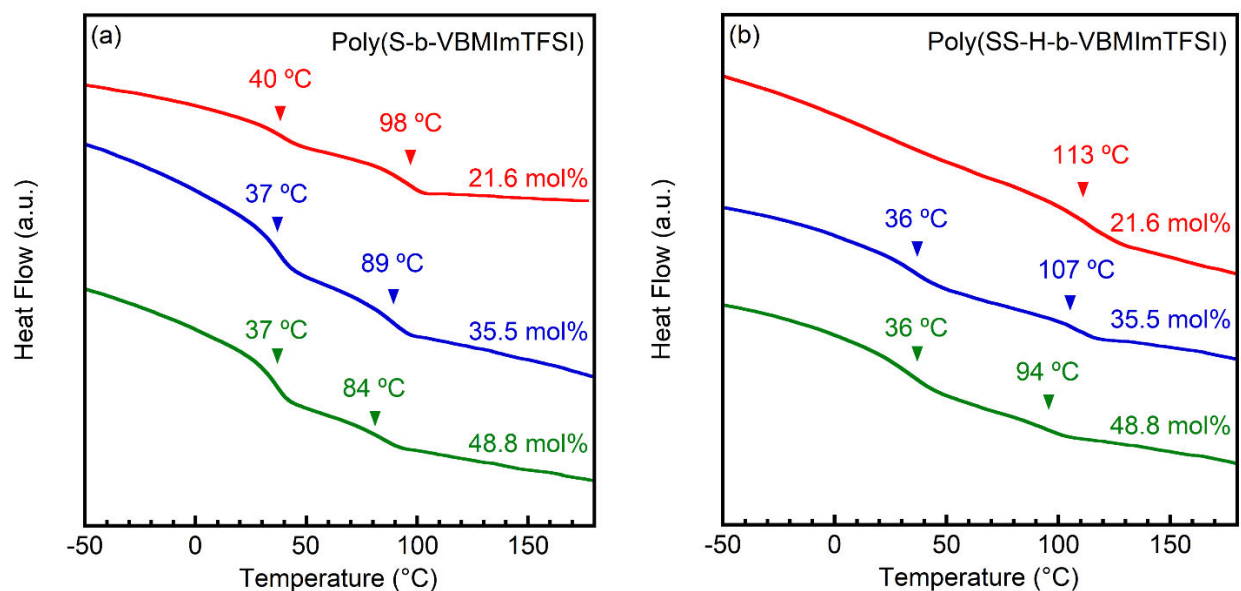


Figure 4. DSC thermograms of (a) non-sulfonated PILBCP (poly(S-*b*-VBMImTFSI)) and (b) sulfonated PILBCP (S-PILBCPs; poly(SS-H-*b*-VBMImTFSI)); PIL molar compositions: 21.6% (red), 35.5% (blue), 48.8% (green).

SAXS profiles of the S-PILBCPs and the corresponding non-sulfonated TFSI-conducting PILBCPs with PIL block molar composition ranging from 21.6% to 48.8% (48.4 to 76.8 vol%) are shown in Figure 5. Bragg peak locations were determined from regression of the profiles using Igor Pro v8.04 (WaveMetrics, Inc) with procedures from Argonne National Laboratory.^{50, 51} The domain spacings (d^*) were determined by $d^* = 2\pi/q^*$ (q^* : primary scattering peak position) and are listed in Table 2. In Figure 5a, the non-sulfonated PILBCPs exhibit multiple scattering peaks at all three PIL compositions, indicating the presence of strong periodic microphase separation supporting the multiple T_{gs} observed in the DSC thermograms (Figure 4). Poly(S-*b*-VBMIm-TFSI-21.6) (PIL block volume fraction of 48.4%) exhibited four scattering peaks at q^* , $\sim\sqrt{3}q^*$, $2q^*$, and $\sim\sqrt{12}q^*$ ($q^* = 0.36 \text{ nm}^{-1}$), suggesting an ordered hexagonal packed cylindrical morphology. Note that, the second and fourth peak q values are slightly different from the ideal Bragg peak location q value (*i.e.*, second peak: $1.57q^*$ (real) vs $1.73q^*$ (ideal); fourth peak: $3.29q^*$ (real) vs $3.46q^*$ (ideal)) due to the broadness of peak deconvoluted from overlapping shoulder and increased noise at higher q positions. The average interdomain spacing was calculated to be 17.3 nm. Note that a different morphology was observed for poly(S-*b*-VBMIm-TFSI-21.6) compared to a PILBCP polymer with similar chemistry and PIL block composition in literature,⁵⁸ which may be attributed to differences in the film processing procedure (*e.g.*, solution casting procedure, substrate, thermal annealing temperature and time). When the volume fraction of PIL block increased to 65.6%, poly(S-*b*-VBMIm-TFSI-35.5) showed four distinct scattering peaks at q^* , $2q^*$, $\sqrt{7}q^*$, and $\sqrt{13}q^*$ ($q^* = 0.35 \text{ nm}^{-1}$), suggesting a hexagonal packed cylindrical morphology with higher long-range order as evidenced by sharper scattering peaks. The average interdomain spacing was calculated to be 17.9 nm. When the PIL block volume fraction further increased to 76.8%, poly(S-*b*-VBMIm-TFSI-48.8) showed four scattering peaks at q^* , $2q^*$, $\sim\sqrt{7}q^*$ and $\sim\sqrt{12}q^*$

($q^* = 0.39 \text{ nm}^{-1}$) again corresponding to a hexagonal packed cylindrical morphology. The morphology and scattering patterns of the non-sulfonated PILBCPs were in good agreement with the literature.⁵⁸ The average interdomain spacing was calculated to be 16.1 nm. With the increase in PIL block composition, the interdomain spacing slightly decreased.

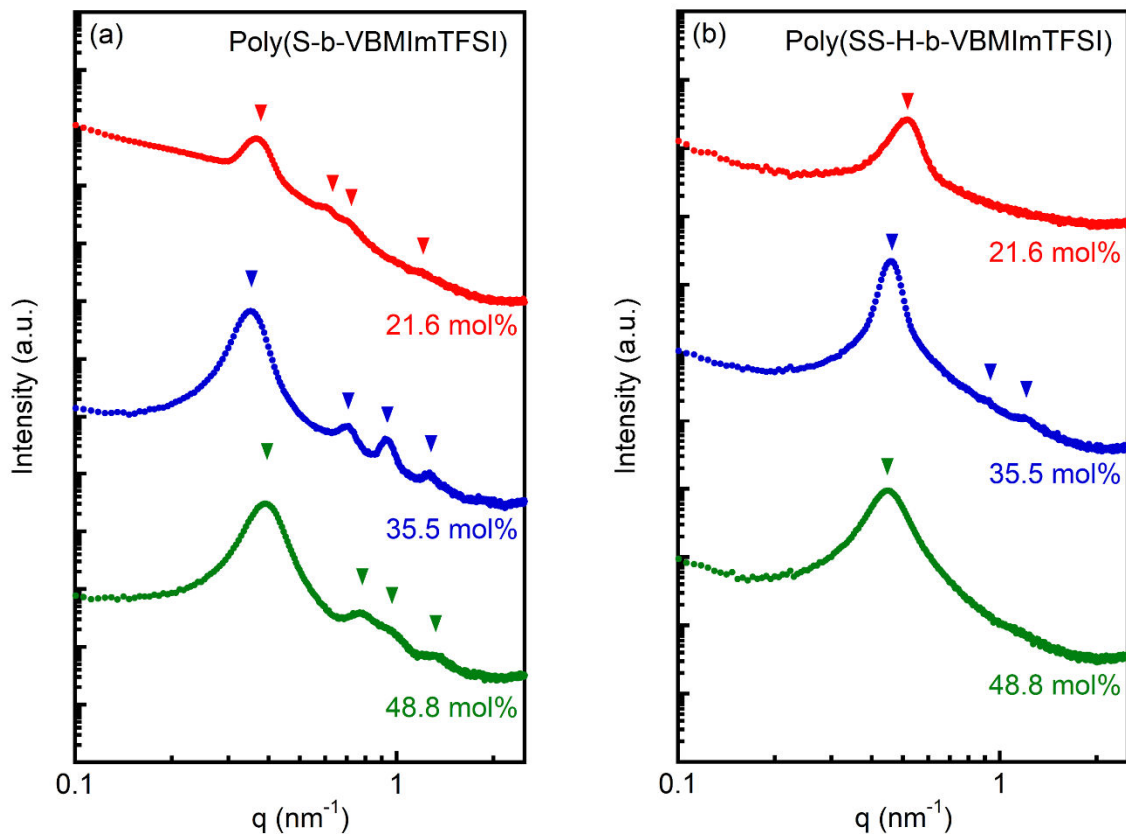


Figure 5. SAXS profiles of (a) non-sulfonated PILBCP (poly(S-*b*-VBMImTFSI)) and (b) sulfonated PILBCP (S-PILBCPs; poly(SS-H-*b*-VBMImTFSI)); PIL molar compositions: 21.6% (red), 35.5% (blue), 48.8% (green).

Table 2. Sulfonated PIL block copolymers morphology and ion transport properties.

S-PILBCPs ^a	interdomain spacing, d^* (nm) ^b	σ^c (mS cm ⁻¹)	S^d (wt%)	water diffusion coefficient (cm ² /s)
Poly(SS-H- <i>b</i> -VBMIIm-TFSI-21.6)	12.2	42.2	21.4	2.15×10^{-7}
Poly(SS-H- <i>b</i> -VBMIIm-TFSI-35.5)	13.7	0.8	8.2	5.03×10^{-7}
Poly(SS-H- <i>b</i> -VBMIIm-TFSI-48.8)	13.9	3.4	7.6	1.02×10^{-6}

^aNumbers correspond to PIL mol % determined from ¹H NMR spectroscopy. ^bCalculated from the primary scattering peak location ($d^* = 2\pi/q^*$) from SAXS profiles. ^cMeasured by EIS at 60 °C and 90% RH. ^dCalculated by water vapor sorption data from DVS at 60 °C and 90% RH. ^eCalculated from the regression of water sorption kinetics data from DVS at 60 °C and 90% RH to Fick's second law.

After sulfonation, poly(SS-H-*b*-VBMIIm-TFSI-21.6) exhibited a broad peak at $q^* = 0.51 \text{ nm}^{-1}$ ($d^* = 12.2 \text{ nm}$), indicating a weak microphase separation without long-range order attributed to the low PIL block composition. For poly(SS-H-*b*-VBMIIm-TFSI-35.5), three scattering peaks were observed at q^* , $2q^*$, and $\sim\sqrt{7}q^*$ ($q^* = 0.46 \text{ nm}^{-1}$), suggesting a hexagonal packed cylindrical morphology. The average interdomain spacing was calculated to be 13.7 nm. Poly(SS-H-*b*-VBMIIm-TFSI-48.8) exhibited a broad peak at $q^* = 0.45 \text{ nm}^{-1}$ ($d^* = 13.9 \text{ nm}$), indicating a weak microphase separation without long-range order. With the increase in PIL block composition, the interdomain spacing of S-PILBCPs slightly increased. Overall, the strength of microphase separation decreased after sulfonation for all three compositions, which might be resulted from the increased ion interaction between the tethered and mobile ions of the two blocks (*i.e.*, complexing between the tethered negatively charged sulfonic acid moieties, the mobile protons, the tethered positively charged imidazolium moieties, and the mobile TFSI anions).

Figure 6a and 6b show the temperature-dependent ion conductivity and water equilibrium sorption under 90% relative humidity (RH), respectively, of the S-PILBCPs with PIL molar compositions ranging from 21.6% to 48.8%. Note that, the high conductivity for the S-PILBCPs

at 90% RH and increasing conductivity with decreasing PIL composition appear to be dominated by the sulfonated block (*i.e.*, proton conduction) due to the inherently hydrophobic PIL block and low mobility of TFSI anion compared to protons. As temperature increases from 40 °C to 80 °C under 90% RH, the conductivity (Figure 6a) increases following an Arrhenius behavior for all three compositions, suggesting a water-assisted ion transport mechanism similar to Nafion as reported in literature.⁵⁹ The conductivity of poly(SS-H-*b*-VBMIm-TFSI-21.6) is comparable to Nafion (*e.g.*, 79.7 mS cm⁻¹ for poly(SS-H-*b*-VBMIm-TFSI-21.6) and 111.2 mS cm⁻¹ for Nafion at 80 °C, respectively). The activation energy of the S-PILBCPs were calculated to be 27.9, 25.8, 13.6 kJ mol⁻¹ for PIL molar compositions of 21.6%, 35.5% and 48.8%, respectively. Interestingly, the conductivity reaches values of 79.7, 1.5, and 4.4 mS cm⁻¹ at 80 °C and 90% RH, following a trend of 21.6 mol% > 48.8 mol% > 35.5 mol%. The conductivity of poly(SS-H-*b*-VBMIm-TFSI-21.6) is significantly higher than poly(SS-H-*b*-VBMIm-TFSI-35.5) and poly(SS-H-*b*-VBMIm-TFSI-48.8), where the latter two achieve similar conductivity despite the difference in PIL block composition.

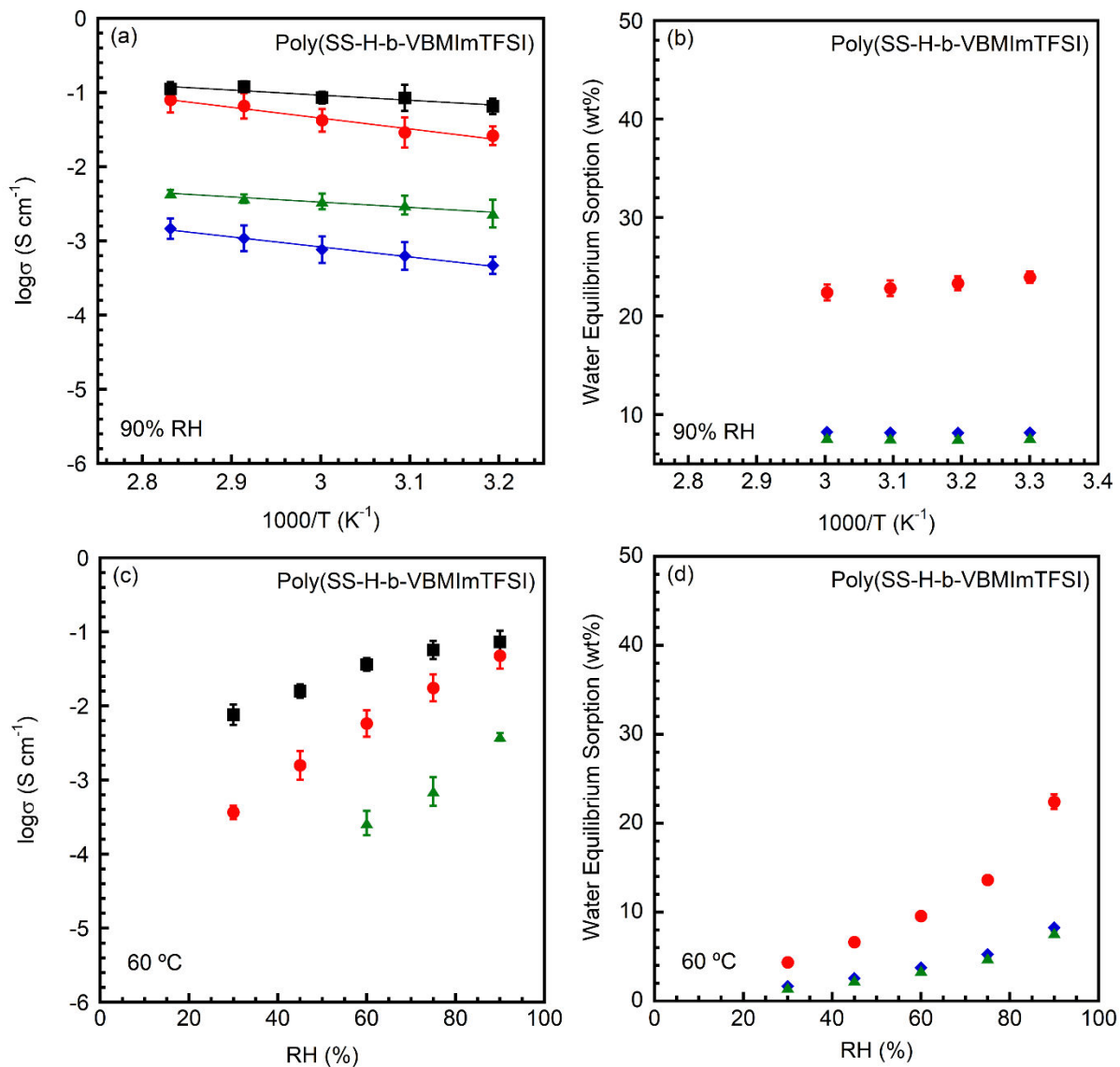


Figure 6. Temperature-dependent (a) ion conductivity and (b) water equilibrium sorption at 90% RH and humidity-dependent (c) ion conductivity and (d) water equilibrium sorption at 60 °C for S-PILBCPs and Nafion (black); PIL molar compositions: 21.6% (red), 35.5% (blue), and 48.8% (green).

Water equilibrium sorption (Figure 6b) remains relatively constant for each polymer at 90% RH in the temperature range of 30 °C - 60 °C. The water sorption of poly(SS-H-*b*-VBMIm-TFSI-21.6)

(*ca.* 21 wt%) is approximately three-fold higher than poly(SS-H-*b*-VBMIm-TFSI-35.5) and poly(SS-H-*b*-VBMIm-TFSI-48.8) (*ca.* 8% for both polymers) for all temperatures, following a similar trend to the conductivity values, suggesting a water-assisted ion transport mechanism of the S-PILBCPs. The higher amount of TFSI anions at higher PIL block composition increases the hydrophobicity of the polymers, resulting in the significant water equilibrium sorption decrease with increasing PIL block compositions. These results indicate that the hydrophobicity and the conductivity of the S-PILBCP can be easily tuned by changing the block composition between sulfonated PS and the PIL.

Figure 6c and 6d show the ion conductivity and water equilibrium sorption of the S-PILPTPs under various relative humidity at 60 °C, respectively. Note that, the conductivity of poly(SS-H-*b*-VBMIm-TFSI-35.5) at all humidity and the conductivity of poly(SS-H-*b*-VBMIm-TFSI-48.8) at 45% RH was not measurable possibly due to the low water sorption and brittleness of the polymer at 60 °C under low relative humidity. The ion conductivity (Figure 6c) of poly(SS-H-*b*-VBMIm-TFSI-21.6) increases by two orders of magnitude (0.4 – 47.7 mS cm⁻¹) with the humidity increase from 30% to 90% RH at 60 °C, and similar trend was observed for poly(SS-H-*b*-VBMIm-TFSI-48.8) from 60% to 90% RH. The water sorption (Figure 6d) increases *ca.* 5-fold with increasing humidity from 30% to 90% RH for all three polymers. Poly(SS-H-*b*-VBMIm-TFSI-21.6) achieved the highest water equilibrium sorption (4.3 – 22.4 wt%) among the polymers, while a similar water sorption increase was observed for poly(SS-H-*b*-VBMIm-TFSI-35.5) (1.6 – 8.2 wt%) and poly(SS-H-*b*-VBMIm-TFSI-48.8) (1.5 – 7.6 wt%). In addition, a similar trend of conductivity versus water content was observed for both poly(SS-H-*b*-VBMIm-TFSI-21.6) and poly(SS-H-*b*-VBMIm-TFSI-48.8) (Figure S7, Supporting Information). This further provides

evidence of the conductivity–water relationship (*i.e.*, conductivity increases with increasing water sorption in the polymer) for the S-PILBCPs.

In addition to ion conductivity and water sorption, water diffusion in S-PILBCPs was investigated *via* DVS experiments over a range of water activities (0 – 0.9) at various temperatures (60, 50, 40, and 30 °C). Figure 7a illustrates one series of water sorption kinetic profiles for poly(SS-H-*b*-VBMIm-TFSI-35.5) at 60 °C responding to the water vapor activity changes (step changes of 0.1 over a range of 0 to 0.9). The water sorption kinetic data were regressed to the solution of Fick’s second law with the appropriate boundary conditions (Equation 3). An example of the regression for one step change for this experiment (water activity: 0 – 0.1) is shown in Figure 7b, where the experimental data match well with the model, suggesting a Fickian diffusion mechanism for water vapor in the S-PILBCPs. The calculated water vapor diffusivity was $6.26 \times 10^{-7} \text{ cm}^2/\text{s}$. All water sorption kinetic profiles at various temperatures in S-PILBCPs with different PIL block compositions were analyzed using the same method.

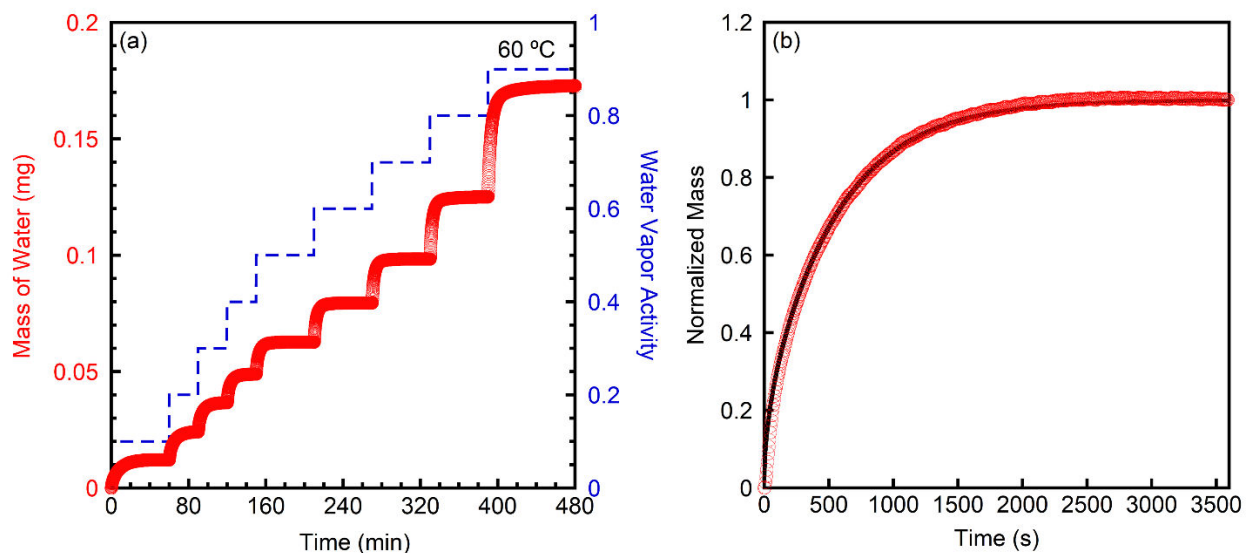


Figure 7. (a) Multiple water vapor sorption kinetic in response to multiple differential external water vapor activity step changes. (b) Water sorption kinetics profile in response to an external water vapor activity step change of 0 to 0.1. The solid black line represents a regression of the experimental data to Equation 3 (Fick's second law), where the diffusion coefficient, D , was the only adjustable parameter. All data for poly(SS-H-*b*-VBMIm-TFSI-35.5) at 60 °C.

Figure 8a shows the average diffusion coefficients from the water sorption kinetic experiments for poly(SS-H-*b*-VBMIm-TFSI-35.5) versus water vapor activity at 60, 50, 40, and 30 °C. The diffusion coefficients increase slightly with increasing temperature at the same water activity (*i.e.*, 1.55×10^{-7} cm²/s at 30 °C to 5.03×10^{-7} cm²/s at 60 °C under a water activity change from 0.8 to 0.9). The average diffusivities at 60, 50, 40, and 30 °C were 7.34×10^{-6} cm²/s, 4.45×10^{-7} cm²/s, 2.92×10^{-7} cm²/s, and 1.81×10^{-7} cm²/s, respectively. The increase of diffusivity from 30 °C to 60 °C could be attributed to a thermal hopping mechanism. At all temperatures, the diffusion coefficients exhibited a fluctuation over the range of water activities, with values ranging from 10^{-6} to 10^{-7} cm²/s, similar in trend to water diffusion in other polymers in literature.⁶⁰⁻⁶³ The values slightly increase with the increase of water vapor activity and reaches a maximum at the water activity of *ca.* 0.6–0.7, then decrease with the increasing water activity from 0.7 to 0.9 (*i.e.*, a parabolic shape). This parabolic behavior and weak dependency of diffusivity on water activity could be attributed to the increasing ionic clustering and the plasticization of the polymers. The increase in diffusion coefficients from water activity of 0 to 0.7 may be attributed to the increasing free volume with increasing water content.⁶³ After the maximum, the diffusivity decreases at higher water vapor activity (0.7–0.9), possibly due to the self-association of water and the

increasing sizes of the water clusters (*i.e.*, the diffusant) with increasing activity, which can slow down diffusion.⁶³⁻⁶⁵

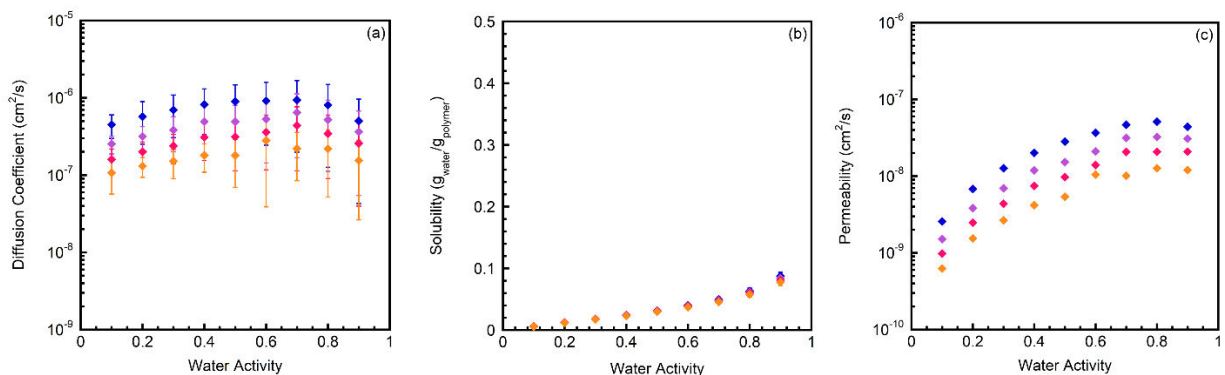


Figure 8. Water vapor (a) diffusion coefficients, (b) solubility, and (c) permeability in poly(SS-H-*b*-VBIm-TFSI-35.5) as a function of water activity at 60 °C (blue), 50 °C (purple), 40 °C (pink), and 30 °C (orange).

Figure 8b shows the water vapor solubility (water vapor mass intake, $g_{\text{water}}/g_{\text{polymer}}$) of poly(SS-H-*b*-VBIm-TFSI-35.5) versus water activity at multiple temperatures. Similar water vapor solubility was observed at the same water activity for all temperatures and the solubility increases with increasing humidity from *ca.* 0.006 (water activity of 0.1) to *ca.* 0.08 $g_{\text{water}}/g_{\text{polymer}}$ (water activity of 0.9). The water vapor permeability was readily calculated by the product of diffusion coefficients and solubility (permeability = diffusivity \times solubility). Figure 8c shows the water vapor permeability versus water activity at multiple temperatures. The permeability increases with increasing temperature following a similar trend as the diffusivity at different temperatures (*i.e.*, solubility remains constant over the temperature range under a specific water activity). At all temperatures, the permeability increases with the increase of water activity and reaches maximum

values at higher water activity values (*ca.* 0.8) compared to that of the diffusion coefficients (*ca.* 0.6 – 0.7), which is due to the continuous increase of water vapor solubility over the water activity range. Similar trend in water transport properties was observed in both poly(SS-H-*b*-VBMIIm-TFSI-21.6) and poly(SS-H-*b*-VBMIIm-TFSI-48.8) (Figure S8 and S9, Supporting Information).

Figure 9 shows the water vapor diffusivity (Figure 9a) and permeability (Figure 9b) versus water activity for S-PILBCPs containing different PIL block compositions. A trend similar to Figure 8a is observed in Figure 9a for S-PILBCPs at all PIL compositions; diffusivity for the water activity step change of 0.8 – 0.9 at 60 °C for all three polymers are shown in Table 2. Interestingly, increasing water diffusion coefficient was observed as PIL block composition increases at all water activity (*i.e.*, poly(SS-H-*b*-VBMIIm-TFSI-48.8) > poly(SS-H-*b*-VBMIIm-TFSI-35.5) > poly(SS-H-*b*-VBMIIm-TFSI-21.6)), most likely due to the fractional free volume increase from the increasing composition of PIL block with large cation and anion sizes. A similar trend has been observed in a study of water vapor diffusion in polymer blends of hydrophobic and hydrophilic polymers, where the diffusion coefficient decreases with the addition of hydrophilic polymers that resulting in lower fractional free volume of the blends.⁶⁶ In Figure 9b, the permeability trend is similar to the diffusivity trend (*i.e.*, permeability increases with increasing PIL block composition). Similar trends for diffusivity and permeability between PIL block compositions were observed at all temperatures (Figure S10, Supporting Information).

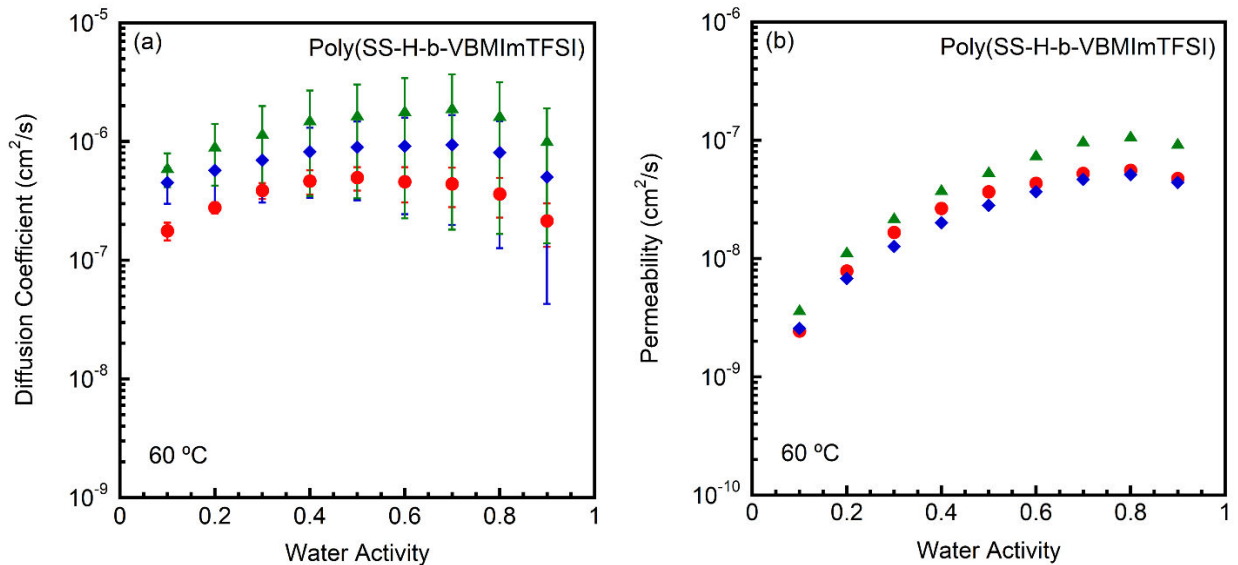


Figure 9. (a) Water vapor diffusion coefficients and (b) water vapor permeability as a function of water activity at 60 °C for S-PILBCPs: poly(SS-H-*b*-VBIm-TFSI-21.6) (red), poly(SS-H-*b*-VBIm-TFSI-35.5) (blue), and poly(SS-H-*b*-VBIm-TFSI-48.8) (green).

In addition, the O₂ transport resistance, ORR activity, and fuel cell performance of MEAs containing S-PILBCPs (from this study) as ionomers were investigated and compared to a MEA containing Nafion as ionomers.^{47, 48} Rotating disk electrode (RDE) half-cell results showed that S-PILBCP thin films with moderate to low thicknesses obtained similar O₂ permeability and O₂ transport resistance compared to Nafion.⁴⁷ In MEA analysis, S-PILBCP only MEA showed higher non-Fickian O₂ transport resistance compared to Nafion-only MEA with similar loading, especially at low RH, due to lower normalized electrochemical active surface area attributed to the limited water uptake and the loss of well-connected proton pathways.⁴⁸ Despite the higher oxygen transport resistance, RDE half-cell results showed an 80% improvement in the ORR activity for S-PILBCP incorporated catalyst layers compared to Nafion ones, and sulfonate adsorption was significantly reduced for the S-PILBCP thin films in comparison to Nafion.⁴⁷ The MEA with S-

PILBCPs showed approximately double the catalyst mass and specific activity compared to those observed for the MEA with Nafion, indicating the impact of S-PILBCPs on the ORR activity improvement.⁴⁸ A substantial enhancement in fuel cell performance was also achieved for the MEA containing Nafion/S-PILBCP mixed ionomers compared to the Nafion only MEA. These promising results suggest that the S-PILBCP not only achieves *ex-situ* ion and water transport properties (*e.g.*, conductivity, water equilibrium sorption) on par with the benchmark Nafion ionomer, but also allows for the modification of the ionomer/catalyst interface, leading to catalytic enhancement and improvement in the overall performance of PEMFCs.

4. Conclusion

In summary, a series of proton-conducting S-PILBCPs containing sulfonic acid moieties in the sulfonated styrene block and IL moieties (VBMIm-TFSI) in the PIL block were successfully synthesized and investigated as a function of block composition. The chemistry of the S-PILBCPs was confirmed by ¹H NMR spectroscopy, ATR-FTIR spectroscopy, and TGA. Hexagonal packed cylindrical morphology was observed for the non-sulfonated PILBCPs, while a weakly microphase separated morphology was observed after sulfonation, *i.e.*, loss in periodicity. High conductivity (79.7 mS cm⁻¹ at 80 °C and 90% RH, comparable to Nafion) with a moderate water content (22 wt% at 60 °C and 90% RH) was achieved at low PIL block composition. Ion conductivity and water content decreased with increasing PIL block composition and water vapor diffusivity and permeability increased with increasing water content and increasing temperature. This work provides valuable insights into the synthesis and transport properties of S-PILBCPs as ionomers for PEMFCs, which ultimately has led to substantial improvement in ORR activity and subsequently fuel cell performance.

Acknowledgements. The authors acknowledge the support from the Department of Energy, Office of Energy Efficiency and Renewable Energy, Hydrogen and Fuel Cell Technologies Office through grant DE-EE0008434. This work was authored in part by Alliance for Sustainable Energy, LLC, the manager and operator of the National Renewable Energy Laboratory for the U.S. Department of Energy (DOE) under Contract No. DE-AC36-08GO28308. Research supported by the U.S. Department of Energy, Office of Energy Efficiency and Renewable Energy, Hydrogen and Fuel Cell Technologies Office (FCTO) through the Million Mile Fuel Cell Truck Consortium. The views expressed in the article do not necessarily represent the views of the DOE or the U.S. Government. The U.S. Government retains and the publisher, by accepting the article for publication, acknowledges that the U.S. Government retains a nonexclusive, paid-up, irrevocable, worldwide license to publish or reproduce the published form of this work, or allow others to do so, for U.S. Government purposes.

Supporting Information: synthesis of the Polystyrene (PS) macro-CTA; SEC chromatograms for PS-CTAs; NMR spectra of S-PILBCPs with PIL block molar composition of 21.6% and 48.8%; EA results of non-sulfonated PILBCPs and S-PILBCPs with PIL block molar composition of 21.6% and 48.8%; density estimation for PILs and volume fraction of PIL Block in PILBCPs; ATR-FTIR spectra and TGA thermograms of S-PILBCPs with PIL block molar composition of 21.6% and 48.8%; conductivity as a function of water equilibrium sorption of S-PILBCPs; water transport of S-PILBCPs with PIL block molar composition of 21.6% and 48.8%; water vapor diffusion coefficients and permeability of S-PILBCPs.

References

1. Wang, Y.; Chen, K. S.; Mishler, J.; Cho, S. C.; Adroher, X. C. A review of polymer electrolyte membrane fuel cells: Technology, applications, and needs on fundamental research. *Applied Energy* **2011**, 88 (4), 981-1007 DOI: <https://doi.org/10.1016/j.apenergy.2010.09.030>.
2. Kongkanand, A.; Mathias, M. F. The Priority and Challenge of High-Power Performance of Low-Platinum Proton-Exchange Membrane Fuel Cells. *The Journal of Physical Chemistry Letters* **2016**, 7 (7), 1127-1137 DOI: 10.1021/acs.jpcclett.6b00216.
3. Debe, M. K. Electrocatalyst approaches and challenges for automotive fuel cells. *Nature* **2012**, 486 (7401), 43-51 DOI: 10.1038/nature11115.
4. Wang, Y.; Ruiz Diaz, D. F.; Chen, K. S.; Wang, Z.; Adroher, X. C. Materials, technological status, and fundamentals of PEM fuel cells – A review. *Materials Today* **2020**, 32, 178-203 DOI: <https://doi.org/10.1016/j.mattod.2019.06.005>.
5. Shao, M.; Chang, Q.; Dodelet, J.-P.; Chenitz, R. Recent Advances in Electrocatalysts for Oxygen Reduction Reaction. *Chem. Rev.* **2016**, 116 (6), 3594-3657 DOI: 10.1021/acs.chemrev.5b00462.
6. Sui, S.; Wang, X.; Zhou, X.; Su, Y.; Riffat, S.; Liu, C.-j. A comprehensive review of Pt electrocatalysts for the oxygen reduction reaction: Nanostructure, activity, mechanism and carbon support in PEM fuel cells. *J. Mater. Chem. A* **2017**, 5 (5), 1808-1825 DOI: 10.1039/C6TA08580F.
7. Li, Y.; Li, Q.; Wang, H.; Zhang, L.; Wilkinson, D. P.; Zhang, J. Recent Progresses in Oxygen Reduction Reaction Electrocatalysts for Electrochemical Energy Applications. *Electrochemical Energy Reviews* **2019**, 2 (4), 518-538 DOI: 10.1007/s41918-019-00052-4.

8. Van Cleve, T.; Wang, G.; Mooney, M.; Cetinbas, C. F.; Kariuki, N.; Park, J.; Farghaly, A.; Myers, D.; Neyerlin, K. C. Tailoring electrode microstructure via ink content to enable improved rated power performance for platinum cobalt/high surface area carbon based polymer electrolyte fuel cells. *Journal of Power Sources* **2021**, 482, 228889 DOI: <https://doi.org/10.1016/j.jpowsour.2020.228889>.
9. Yarlalagadda, V.; Carpenter, M. K.; Moylan, T. E.; Kukreja, R. S.; Koestner, R.; Gu, W.; Thompson, L.; Kongkanand, A. Boosting Fuel Cell Performance with Accessible Carbon Mesopores. *ACS Energy Letters* **2018**, 3 (3), 618-621 DOI: 10.1021/acseenergylett.8b00186.
10. Hwang, M.; Elabd, Y. A. Impact of ionomer resistance in nanofiber-nanoparticle electrodes for ultra-low platinum fuel cells. *Int. J. Hydrogen Energy* **2019**, 44 (12), 6245-6256 DOI: <https://doi.org/10.1016/j.ijhydene.2019.01.083>.
11. O'Hayre, R.; Barnett, D. M.; Prinz, F. B. The Triple Phase Boundary: A Mathematical Model and Experimental Investigations for Fuel Cells. *J. Electrochem. Soc.* **2005**, 152 (2), A439-A444 DOI: 10.1149/1.1851054.
12. Weber, A. Z.; Kusoglu, A. Unexplained transport resistances for low-loaded fuel-cell catalyst layers. *J. Mater. Chem. A* **2014**, 2 (41), 17207-17211 DOI: 10.1039/C4TA02952F.
13. Kim, Y. S. Polymer Electrolytes with High Ionic Concentration for Fuel Cells and Electrolyzers. *ACS Applied Polymer Materials* **2021**, 3 (3), 1250-1270 DOI: 10.1021/acsapm.0c01405.
14. Snyder, J.; Fujita, T.; Chen, M. W.; Erlebacher, J. Oxygen reduction in nanoporous metal-ionic liquid composite electrocatalysts. *Nat. Mater.* **2010**, 9 (11), 904-907 DOI: 10.1038/nmat2878.

15. Zhang, G.-R.; Munoz, M.; Etzold, B. J. M. Boosting Performance of Low Temperature Fuel Cell Catalysts by Subtle Ionic Liquid Modification. *ACS Appl. Mater. Interfaces* **2015**, *7* (6), 3562-3570 DOI: 10.1021/am5074003.
16. Zhang, G.-R.; Wolker, T.; Sandbeck, D. J. S.; Munoz, M.; Mayrhofer, K. J. J.; Cherevko, S.; Etzold, B. J. M. Tuning the Electrocatalytic Performance of Ionic Liquid Modified Pt Catalysts for the Oxygen Reduction Reaction via Cationic Chain Engineering. *ACS Catalysis* **2018**, *8* (9), 8244-8254 DOI: 10.1021/acscatal.8b02018.
17. Huang, K.; Song, T.; Morales-Collazo, O.; Jia, H.; Brennecke, J. F. Enhancing Pt/C Catalysts for the Oxygen Reduction Reaction with Protic Ionic Liquids: The Effect of Anion Structure. *J. Electrochem. Soc.* **2017**, *164* (13), F1448-F1459 DOI: 10.1149/2.1071713jes.
18. Li, Y.; Hart, J.; Profitt, L.; Intikhab, S.; Chatterjee, S.; Taheri, M.; Snyder, J. Sequential Capacitive Deposition of Ionic Liquids for Conformal Thin Film Coatings on Oxygen Reduction Reaction Electrocatalysts. *ACS Catalysis* **2019**, *9* (10), 9311-9316 DOI: 10.1021/acscatal.9b03157.
19. Snyder, J.; Livi, K.; Erlebacher, J. Oxygen Reduction Reaction Performance of [MTBD][beti]-Encapsulated Nanoporous NiPt Alloy Nanoparticles. *Adv. Funct. Mater.* **2013**, *23* (44), 5494-5501 DOI: 10.1002/adfm.201301144.
20. Zhang, G.-R.; Etzold, B. J. M. Ionic liquids in electrocatalysis. *Journal of Energy Chemistry* **2016**, *25* (2), 199-207 DOI: <https://doi.org/10.1016/j.jechem.2016.01.007>.
21. Qiao, M.; Tang, C.; Tanase, L. C.; Teodorescu, C. M.; Chen, C.; Zhang, Q.; Titirici, M.-M. Oxygenophilic ionic liquids promote the oxygen reduction reaction in Pt-free carbon electrocatalysts. *Mater. Horizons* **2017**, *4* (5), 895-899 DOI: 10.1039/C7MH00298J.

22. Qiao, M.; Ferrero, G. A.; Fernández Velasco, L.; Vern Hor, W.; Yang, Y.; Luo, H.; Lodewyckx, P.; Fuertes, A. B.; Sevilla, M.; Titirici, M.-M. Boosting the Oxygen Reduction Electrocatalytic Performance of Nonprecious Metal Nanocarbons via Triple Boundary Engineering Using Protic Ionic Liquids. *ACS Appl. Mater. Interfaces* **2019**, 11 (12), 11298-11305 DOI: 10.1021/acsami.8b18375.
23. Zhang, G.-R.; Munoz, M.; Etzold, B. J. M. Accelerating Oxygen-Reduction Catalysts through Preventing Poisoning with Non-Reactive Species by Using Hydrophobic Ionic Liquids. *Angewandte Chemie International Edition* **2016**, 55 (6), 2257-2261 DOI: 10.1002/anie.201508338.
24. Li, Y.; Intikhab, S.; Malkani, A.; Xu, B.; Snyder, J. Ionic Liquid Additives for the Mitigation of Nafion Specific Adsorption on Platinum. *ACS Catalysis* **2020**, 10 (14), 7691-7698 DOI: 10.1021/acscatal.0c01243.
25. Subbaraman, R.; Strmcnik, D.; Paulikas, A. P.; Stamenkovic, V. R.; Markovic, N. M. Oxygen Reduction Reaction at Three-Phase Interfaces. *ChemPhysChem* **2010**, 11 (13), 2825-2833 DOI: <https://doi.org/10.1002/cphc.201000190>.
26. Van Cleve, T.; Khandavalli, S.; Chowdhury, A.; Medina, S.; Pylypenko, S.; Wang, M.; More, K. L.; Kariuki, N.; Myers, D. J.; Weber, A. Z.; Mauger, S. A.; Ulsh, M.; Neyerlin, K. C. Dictating Pt-Based Electrocatalyst Performance in Polymer Electrolyte Fuel Cells, from Formulation to Application. *ACS Appl. Mater. Interfaces* **2019**, 11 (50), 46953-46964 DOI: 10.1021/acsami.9b17614.
27. Masuda, T.; Ikeda, K.; Uosaki, K. Potential-Dependent Adsorption/Desorption Behavior of Perfluorosulfonated Ionomer on a Gold Electrode Surface Studied by Cyclic Voltammetry,

Electrochemical Quartz Microbalance, and Electrochemical Atomic Force Microscopy.

Langmuir **2013**, 29 (7), 2420-2426 DOI: 10.1021/la304705k.

28. Hickner, M. A.; Ghassemi, H.; Kim, Y. S.; Einsla, B. R.; McGrath, J. E. Alternative Polymer Systems for Proton Exchange Membranes (PEMs). *Chem. Rev.* **2004**, 104 (10), 4587-4612 DOI: 10.1021/cr020711a.

29. Elabd, Y. A.; Hickner, M. A. Block Copolymers for Fuel Cells. *Macromolecules* **2011**, 44 (1), 1-11 DOI: 10.1021/ma101247c.

30. Liu, Y.-L. Developments of highly proton-conductive sulfonated polymers for proton exchange membrane fuel cells. *Polymer Chemistry* **2012**, 3 (6), 1373-1383 DOI: 10.1039/C2PY20106B.

31. Kang, S.; Park, M. J. 100th Anniversary of Macromolecular Science Viewpoint: Block Copolymers with Tethered Acid Groups: Challenges and Opportunities. *ACS Macro Lett.* **2020**, 9 (11), 1527-1541 DOI: 10.1021/acsmacrolett.0c00629.

32. Hwang, M.; Nixon, K.; Sun, R.; Willis, C.; Elabd, Y. A. Sulfonated pentablock terpolymers as membranes and ionomers in hydrogen fuel cells. *J. Membr. Sci.* **2021**, 633, 119330 DOI: <https://doi.org/10.1016/j.memsci.2021.119330>.

33. Hu, Y.; Li, X.; Yan, L.; Yue, B. Improving the Overall Characteristics of Proton Exchange Membranes via Nanophase Separation Technologies: A Progress Review. *Fuel Cells* **2017**, 17 (1), 3-17 DOI: <https://doi.org/10.1002/fuce.201600172>.

34. Date, B.; Han, J.; Park, S.; Park, E. J.; Shin, D.; Ryu, C. Y.; Bae, C. Synthesis and Morphology Study of SEBS Triblock Copolymers Functionalized with Sulfonate and Phosphonate Groups for Proton Exchange Membrane Fuel Cells. *Macromolecules* **2018**, 51 (3), 1020-1030 DOI: 10.1021/acs.macromol.7b01848.

35. Yuan, J. Y.; Antonietti, M. Poly(ionic liquid)s: Polymers expanding classical property profiles. *Polymer* **2011**, 52 (7), 1469-1482 DOI: 10.1016/j.polymer.2011.01.043.
36. Yuan, J. Y.; Mecerreyes, D.; Antonietti, M. Poly(ionic liquid)s: An update. *Prog. Polym. Sci.* **2013**, 38 (7), 1009-1036 DOI: 10.1016/j.progpolymsci.2013.04.002.
37. Meek, K. M.; Elabd, Y. A. Polymerized ionic liquid block copolymers for electrochemical energy. *J. Mater. Chem. A* **2015**, 3 (48), 24187-24194 DOI: 10.1039/c5ta07170d.
38. Qian, W.; Texter, J.; Yan, F. Frontiers in poly(ionic liquid)s: syntheses and applications. *Chem. Soc. Rev.* **2017**, 46 (4), 1124-1159 DOI: 10.1039/C6CS00620E.
39. Chen, T.-L.; Sun, R.; Willis, C.; Morgan, B. F.; Beyer, F. L.; Elabd, Y. A. Lithium ion conducting polymerized ionic liquid pentablock terpolymers as solid-state electrolytes. *Polymer* **2019**, 161, 128-138 DOI: <https://doi.org/10.1016/j.polymer.2018.12.013>.
40. Nykaza, J. R.; Benjamin, R.; Meek, K. M.; Elabd, Y. A. Polymerized ionic liquid diblock copolymer as an ionomer and anion exchange membrane for alkaline fuel cells. *Chemical Engineering Science* **2016**, 154, 119-127 DOI: <https://doi.org/10.1016/j.ces.2016.05.041>.
41. Sun, R.; Elabd, Y. A. Synthesis and High Alkaline Chemical Stability of Polyionic Liquids with Methylpyrrolidinium, Methylpiperidinium, Methylazepanium, Methylazocanium, and Methylazonanium Cations. *ACS Macro Lett.* **2019**, 8 (5), 540-545 DOI: 10.1021/acsmacrolett.9b00039.
42. Meek, K. M.; Sun, R.; Willis, C.; Elabd, Y. A. Hydroxide conducting polymerized ionic liquid pentablock terpolymer anion exchange membranes with methylpyrrolidinium cations. *Polymer* **2018**, 134, 221-226 DOI: <https://doi.org/10.1016/j.polymer.2017.11.050>.

43. Chen, T.-L.; Lathrop, P. M.; Sun, R.; Elabd, Y. A. Lithium-Ion Transport in Poly(ionic liquid) Diblock Copolymer Electrolytes: Impact of Salt Concentration and Cation and Anion Chemistry. *Macromolecules* **2021**, 54 (18), 8780-8797 DOI: 10.1021/acs.macromol.1c00694.
44. Chen, T.-L.; Sun, R.; Willis, C.; Krutzer, B.; Morgan, B. F.; Beyer, F. L.; Han, K. S.; Murugesan, V.; Elabd, Y. A. Impact of ionic liquid on lithium ion battery with a solid poly(ionic liquid) pentablock terpolymer as electrolyte and separator. *Polymer* **2020**, 209, 122975 DOI: <https://doi.org/10.1016/j.polymer.2020.122975>.
45. Hwang, M.; Sun, R.; Willis, C.; Elabd, Y. A. Solid-State Alkaline Fuel Cell Performance of Pentablock Terpolymer with Methylpyrrolidinium Cations as Anion Exchange Membrane and Ionomer. *Fuel Cells* **2020**, 20 (5), 624-633 DOI: <https://doi.org/10.1002/fuce.202000092>.
46. Meek, K. M.; Elabd, Y. A. Sulfonated Polymerized Ionic Liquid Block Copolymers. *Macromol. Rapid Commun.* **2016**, 37 (14), 1200-1206 DOI: 10.1002/marc.201600089.
47. Gawas, R.; Sun, R.; Li, Y.; Neyerlin, K. C.; Elabd, Y. A.; Tang, M.; Snyder, J. Characterization of a Sulfonated Poly(Ionic Liquid) Block Copolymer as an Ionomer for Proton Exchange Membrane Fuel Cells using Rotating Disk Electrode. *J. Electrochem. Soc.* **2021**, 168 (12), 124511 DOI: 10.1149/1945-7111/ac4375.
48. Li, Y.; Van Cleve, T.; Sun, R.; Gawas, R.; Wang, G.; Tang, M.; Elabd, Y. A.; Snyder, J.; Neyerlin, K. C. Modifying the Electrocatalyst–Ionomer Interface via Sulfonated Poly(ionic liquid) Block Copolymers to Enable High-Performance Polymer Electrolyte Fuel Cells. *ACS Energy Letters* **2020**, 5 (6), 1726-1731 DOI: 10.1021/acseenergylett.0c00532.
49. Elabd, Y. A.; Napadensky, E. Sulfonation and characterization of poly(styrene-isobutylene-styrene) triblock copolymers at high ion-exchange capacities. *Polymer* **2004**, 45 (9), 3037-3043 DOI: <https://doi.org/10.1016/j.polymer.2004.02.061>.

50. Ilavsky, J.; Jemian, P. R. Irena: tool suite for modeling and analysis of small-angle scattering. *Journal of Applied Crystallography* **2009**, 42 (2), 347-353 DOI: doi:10.1107/S0021889809002222.
51. Ilavsky, J. Nika: software for two-dimensional data reduction. *Journal of Applied Crystallography* **2012**, 45 (2), 324-328 DOI: doi:10.1107/S0021889812004037.
52. Davis, E. M.; Theryo, G.; Hillmyer, M. A.; Cairncross, R. A.; Elabd, Y. A. Liquid Water Transport in Polylactide Homo and Graft Copolymers. *ACS Appl. Mater. Interfaces* **2011**, 3 (10), 3997-4006 DOI: 10.1021/am2008618.
53. Preda, F.-M.; Alegría, A.; Bocahut, A.; Fillot, L.-A.; Long, D. R.; Sotta, P. Investigation of Water Diffusion Mechanisms in Relation to Polymer Relaxations in Polyamides. *Macromolecules* **2015**, 48 (16), 5730-5741 DOI: 10.1021/acs.macromol.5b01295.
54. Kiefer, J.; Fries, J.; Leipertz, A. Experimental Vibrational Study of Imidazolium-Based Ionic Liquids: Raman and Infrared Spectra of 1-Ethyl-3-methylimidazolium Bis(Trifluoromethylsulfonyl)imide and 1-Ethyl-3-methylimidazolium Ethylsulfate. *Applied Spectroscopy* **2007**, 61 (12), 1306-1311 DOI: 10.1366/000370207783292000.
55. Rey, I.; Johansson, P.; Lindgren, J.; Lassègues, J. C.; Grondin, J.; Servant, L. Spectroscopic and Theoretical Study of (CF₃SO₂)₂N⁻ (TFSI⁻) and (CF₃SO₂)₂NH (HTFSI). *J. Phys. Chem. A* **1998**, 102 (19), 3249-3258 DOI: 10.1021/jp980375v.
56. Weiss, R. A.; Sen, A.; Willis, C. L.; Pottick, L. A. Block copolymer ionomers: 1. Synthesis and physical properties of sulphonated poly(styrene-ethylene/butylene-styrene). *Polymer* **1991**, 32 (10), 1867-1874 DOI: [https://doi.org/10.1016/0032-3861\(91\)90378-V](https://doi.org/10.1016/0032-3861(91)90378-V).
57. Suleiman, D.; Napadensky, E.; Sloan, J. M.; Crawford, D. M. Thermogravimetric characterization of highly sulfonated poly(styrene–isobutylene–styrene) block copolymers:

Effects of sulfonation and counter-ion substitution. *Thermochim. Acta* **2007**, 460 (1), 35-40 DOI: <https://doi.org/10.1016/j.tca.2007.05.012>.

58. May, A. W.; Shi, Z.; Wijayasekara, D. B.; Gin, D. L.; Bailey, T. S. Self-assembly of highly asymmetric, poly(ionic liquid)-rich diblock copolymers and the effects of simple structural modification on phase behaviour. *Polymer Chemistry* **2019**, 10 (6), 751-765 DOI: 10.1039/C8PY01414K.

59. Hsu, W. Y.; Barkley, J. R.; Meakin, P. Ion Percolation and Insulator-to-Conductor Transition in Nafion Perfluorosulfonic Acid Membranes. *Macromolecules* **1980**, 13 (1), 198-200 DOI: 10.1021/ma60073a041.

60. Hallinan, D. T.; De Angelis, M. G.; Giacinti Baschetti, M.; Sarti, G. C.; Elabd, Y. A. Non-Fickian Diffusion of Water in Nafion. *Macromolecules* **2010**, 43 (10), 4667-4678 DOI: 10.1021/ma100047z.

61. Morris, D. R.; Sun, X. Water-sorption and transport properties of Nafion 117 H. *J Appl Polym Sci* **1993**, 50 (8), 1445-1452 DOI: <https://doi.org/10.1002/app.1993.070500816>.

62. Burnett, D. J.; Garcia, A. R.; Thielmann, F. Measuring moisture sorption and diffusion kinetics on proton exchange membranes using a gravimetric vapor sorption apparatus. *Journal of Power Sources* **2006**, 160 (1), 426-430 DOI: <https://doi.org/10.1016/j.jpowsour.2005.12.096>.

63. Davis, E. M.; Elabd, Y. A. Water Clustering in Glassy Polymers. *The Journal of Physical Chemistry B* **2013**, 117 (36), 10629-10640 DOI: 10.1021/jp405388d.

64. Wellons, J. D.; Stannett, V. Permeation, sorption, and diffusion of water in ethyl cellulose. *Journal of Polymer Science Part A-1: Polymer Chemistry* **1966**, 4 (3), 593-602 DOI: <https://doi.org/10.1002/pol.1966.150040313>.

65. Nguyen, Q. T.; Favre, E.; Ping, Z. H.; Néel, J. Clustering of solvents in membranes and its influence on membrane transport properties. *J. Membr. Sci.* **1996**, 113 (1), 137-150 DOI: [https://doi.org/10.1016/0376-7388\(95\)00219-7](https://doi.org/10.1016/0376-7388(95)00219-7).
66. Schult, K. A.; Paul, D. R. Water sorption and transport in blends of polyethyloxazoline and polyethersulfone. *Journal of Polymer Science Part B: Polymer Physics* **1997**, 35 (6), 993-1007 DOI: [https://doi.org/10.1002/\(SICI\)1099-0488\(19970430\)35:6<993::AID-POLB13>3.0.CO;2-A](https://doi.org/10.1002/(SICI)1099-0488(19970430)35:6<993::AID-POLB13>3.0.CO;2-A).

